Cryo-EM of elongating ribosome with EF-Tu•GTP elucidates tRNA proofreading

https://doi.org/10.1038/s41586-020-2447-x

Received: 30 August 2019

Accepted: 10 April 2020

Published online: 1 July 2020

Check for updates

Anna B. Loveland[1], Gabriel Demo[1,2] & Andrei A. Korostelev[1]✉

Ribosomes accurately decode mRNA by proofreading each aminoacyl-tRNA that is delivered by the elongation factor EF-Tu[1]. To understand the molecular mechanism of this proofreading step it is necessary to visualize GTP-catalysed elongation, which has remained a challenge[2–4]. Here we use time-resolved cryogenic electron microscopy to reveal 33 ribosomal states after the delivery of aminoacyl-tRNA by EF-Tu•GTP. Instead of locking cognate tRNA upon initial recognition, the ribosomal decoding centre dynamically monitors codon–anticodon interactions before and after GTP hydrolysis. GTP hydrolysis enables the GTPase domain of EF-Tu to extend away, releasing EF-Tu from tRNA. The 30S subunit then locks cognate tRNA in the decoding centre and rotates, enabling the tRNA to bypass 50S protrusions during accommodation into the peptidyl transferase centre. By contrast, the decoding centre fails to lock near-cognate tRNA, enabling the dissociation of near-cognate tRNA both during initial selection (before GTP hydrolysis) and proofreading (after GTP hydrolysis). These findings reveal structural similarity between ribosomes in initial selection states[5,6] and in proofreading states, which together govern the efficient rejection of incorrect tRNA.

A translating ribosome selects an appropriate aminoacyl-tRNA (aa-tRNA) and connects the incoming amino acid to the elongating peptide chain. The aa-tRNA binds the ribosome as a ternary complex with elongation factor Tu (EF-Tu) and GTP (Fig. 1a; reviewed in refs. [2–4]). The selection of an appropriate tRNA involves two steps: initial selection and proofreading[1]. Initial selection discriminates against non-cognate tRNAs in the 30S A site before EF-Tu hydrolyses GTP, allowing the intact non-cognate aa-tRNA•EF-Tu•GTP ternary complex to dissociate from the ribosome[2–4]. GTP hydrolysis releases EF-Tu•GDP from the tRNA acceptor arm, which travels through the intersubunit space and inserts (accommodates) into the peptidyl transferase centre (PTC) on the 50S subunit[7–9]. After GTP hydrolysis and before peptidyl transfer, the ribosome proofreads the aa-tRNA to reject incorrectly selected near-cognate aa-tRNA, thus preventing elongation with an incorrect amino acid[1,10,11].

Structural visualization of GTP-catalysed decoding has been challenging, so high-resolution structures of decoding complexes have typically been captured by blocking GTP hydrolysis and elongation[5,6,12,13] (see Supplementary Discussion). Many structural steps remain to be captured in order to answer long-standing questions. First, it is not known how the ribosome initially selects an incorrect near-cognate tRNA but then rejects it by proofreading before forming a peptide bond. Next, it remains to be seen how GTP hydrolysis facilitates the dissociation of EF-Tu, and whether the dissociating EF-Tu could drive tRNA accommodation via a power-stroke-like mechanism[14]. Finally, it is unclear how tRNA bypasses structural obstacles[15] in order to accommodate in the A site. To answer these questions, structural intermediates in the elongation pathway must be visualized using authentic substrates.

Here we used cryogenic electron microscopy (cryo-EM) to visualize an elongation event catalysed by EF-Tu•GTP (Fig. 1a). aa-tRNA was delivered as an aa-tRNA•EF-Tu•GTP ternary complex to the 70S initiation ribosome programmed with a cognate or a near-cognate mRNA codon in the A site. Cryo-EM data classification revealed numerous functional states (see Methods). We describe 17 structures of the ribosome with cognate tRNA (average resolutions of 3.0 Å to 4.0 Å) (Fig. 1b, Extended Data Fig. 1), and 16 states of the near-cognate ribosome complex (average resolutions of 3.3 Å to 4.3 Å) (Extended Data Fig. 2). These structural ensembles provide a detailed view of elongation (Supplementary Video 1)—including initial selection, GTP hydrolysis, conformational changes in EF-Tu, tRNA proofreading, tRNA accommodation, peptide bond formation and pre-translocation—that to our knowledge is unprecedented. A comparison between cognate and near-cognate elongation reveals the mechanism of proofreading, which is critical for translation fidelity.

Time-resolved cryo-EM reveals EF-Tu intermediates

To identify structural intermediates of elongation with cognate Phe-tRNA^{Phe}, we performed ensemble cryo-EM[16] of the EF-Tu•GTP-catalysed reaction (Fig. 1a) at several time points, consistent with a biochemical time course under similar conditions[17] (Fig. 1c, Methods). Maximum-likelihood classification resolved distinct 70S functional states corresponding to substrates (vacant A site), EF-Tu-bound intermediates (A/T tRNA and EF-Tu) and products (after EF-Tu release) of the decoding and elongation reactions (Fig. 1b–g, Extended Data Fig. 1). Over time, substrate levels decrease and products

[1]RNA Therapeutics Institute, Department of Biochemistry and Molecular Pharmacology, University of Massachusetts Medical School, Worcester, MA, USA. [2]Present address: Central European Institute of Technology, Masaryk University, Brno, Czech Republic. ✉e-mail: andrei.korostelev@umassmed.edu

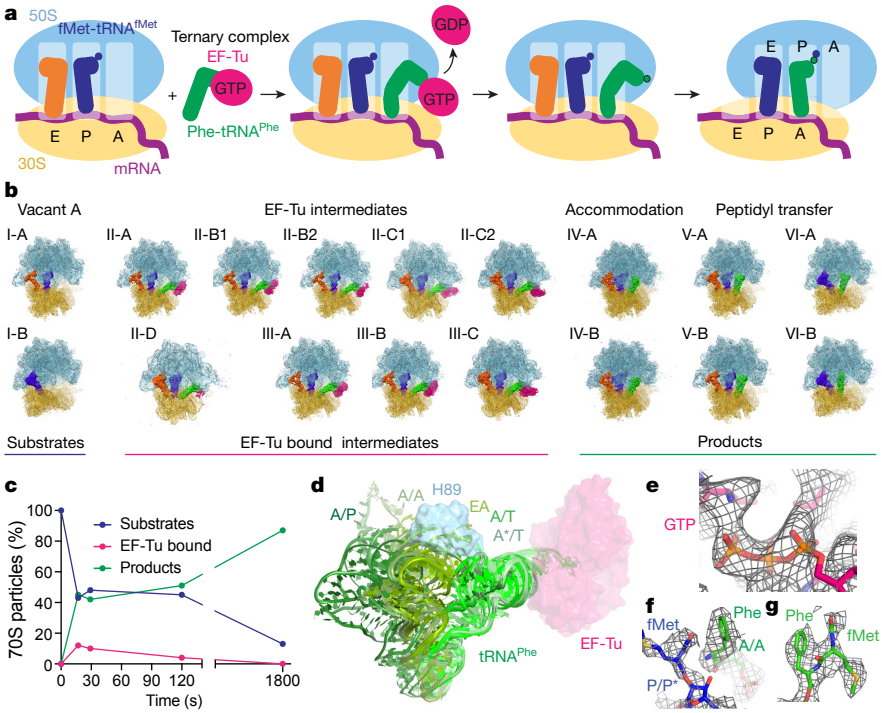

Fig. 1 | Cryo-EM of an elongation event reveals structural intermediates. **a**, Scheme of the reaction of the initiation 70S•fMet-tRNA^{fMet} complex with the cognate Phe-tRNA^{Phe}•EF-Tu•GTP complex to form dipeptidyl fMet-Phe-tRNA. **b**, Cryo-EM maps of 17 states of the elongation reaction, and their assignment as substrates, EF-Tu-bound intermediates or products of the reaction. The maps are coloured to show the 50S ribosomal subunit (light blue), 30S ribosomal subunit (yellow), E-tRNA (orange), P-tRNA (dark blue), A-tRNA (green) and EF-Tu (magenta). **c**, Relative abundance of substrates, EF-Tu intermediates and products over time, obtained from particle distributions in cryo-EM datasets. **d**, Conformations of the incoming tRNA in 17 structures, starting from EF-Tu bound A*/T states (light green tRNA and magenta EF-Tu) to elbow-accommodated (EA) to pre-translocation A/P states (dark green). **e**, Cryo-EM density (mesh) consistent with GTP in the EF-Tu GTPase centre of a transient early state of mRNA decoding (open 30S). **f**, Cryo-EM density of a transient state in the peptidyl transferase centre consistent with aa-tRNA substrates. **g**, Cryo-EM density for fMet-Phe dipeptidyl-tRNA, the product of peptidyl transfer.

accumulate, whereas the EF-Tu-bound states accumulate and then disappear, as expected for reaction intermediates (Fig. 1c). Our approach therefore captures transient states of aa-tRNA delivery catalysed by EF-Tu and GTP (Fig. 1d).

To visualize the structural intermediates of elongation, we focused on high-resolution maps from the 29-second time point (Methods, Extended Data Fig. 1, Supplementary Table 1, Supplementary Table 2), at which EF-Tu-bound particles reach a near-maximum level and peptidyl-transfer products begin to accumulate (Fig. 1c; see additional discussion in Methods). Most maps resolve near-atomic-resolution details (Fig. 1e–g) in the ribosome core and lower-resolution features at the periphery, enabling interpretation of secondary-structure and/or domain rearrangements of EF-Tu (Extended Data Figs. 3–5, 8, 9). Six categories of structure describe distinct functional states (Fig. 1b): substrates I-A and I-B, similar to A-site vacant 70S structures described previously[18,19] (Methods); EF-Tu-bound intermediates II-A to II-D and III-A to III-C (Fig. 2); tRNA accommodation-like states IV-A and IV-B (Fig. 3); peptidyl-transfer classical states V-A and V-B (Fig. 3); and pre-translocation hybrid states VI-A and VI-B (Fig. 3). Collectively, the 17 structures suggest a pathway for cognate aa-tRNA—from its initial binding to the ribosome, through to accommodation, peptide-bond formation and on to pre-translocation (Fig. 1d, Supplementary Video 1).

30S samples open states during EF-Tu rearrangement

EF-Tu contributes to the initial selection, proofreading[20] and accommodation[21] of tRNA, but the structural mechanisms of the latter two processes are unknown. Initial selection is achieved by separating the EF-Tu GTPase (domain 1) from the 50S sarcin–ricin loop (SRL) until the cognate tRNA is recognized in the 30S decoding centre. Recognition of the tRNA anticodon causes a 30S-shoulder shift that docks EF-Tu at the SRL, catalysing GTP hydrolysis (see below and refs. [5,6]). How EF-Tu rearranges and dissociates after GTP hydrolysis is less well understood. Biochemical studies have yielded conflicting results, suggesting that large-scale rearrangements of EF-Tu occur either on the ribosome[22] or after dissociation from the ribosome[23]. It is also unclear whether EF-Tu dynamics facilitate spontaneous or power-stroke-driven accommodation of tRNA into the PTC[14] (Supplementary Information). Isolated EF-Tu adopts two globally different conformations: a compact GTP-bound form and an extended GDP-bound form[24–26]. In the extended conformation, the GTPase domain is rotated by approximately 90°, concurrent with the rearrangement of the switch I (amino acids 38–64) and switch II (amino acids 83–97) regions that outline the GTP-binding pocket[24–26]. However, the available structures of ribosome-bound EF-Tu complexes feature only compact EF-Tu[5,6,12,13,27].

We found three categories of EF-Tu-bound states (nine maps), which suggest the stepwise dissociation of EF-Tu from tRNA. First, in five maps (II-A, II-B1, II-B2, III-A and III-B), EF-Tu adopts a compact conformation that resembles the GTP-bound state but features different conformations of switch regions, indicating distinct states of the GTP-binding pocket (Fig. 2a, b, Extended Data Fig. 3a–f, m, n, p, q). Sub-classification reveals a subset of states, in which EF-Tu interacts with the N-terminal domain of L11 and with L7/L12 (Extended Data Fig. 3s–v, Supplementary Information), consistent with stochastic binding of these 50S proteins[28]. Second, in three maps (II-C1, II-C2 and III-C), EF-Tu adopts extended conformations that resemble the GDP-bound state, in which domain 1 (amino acids 1–200) is released from domain 2 (amino acids 201–299) and rotated by up to around 90° from its position in the

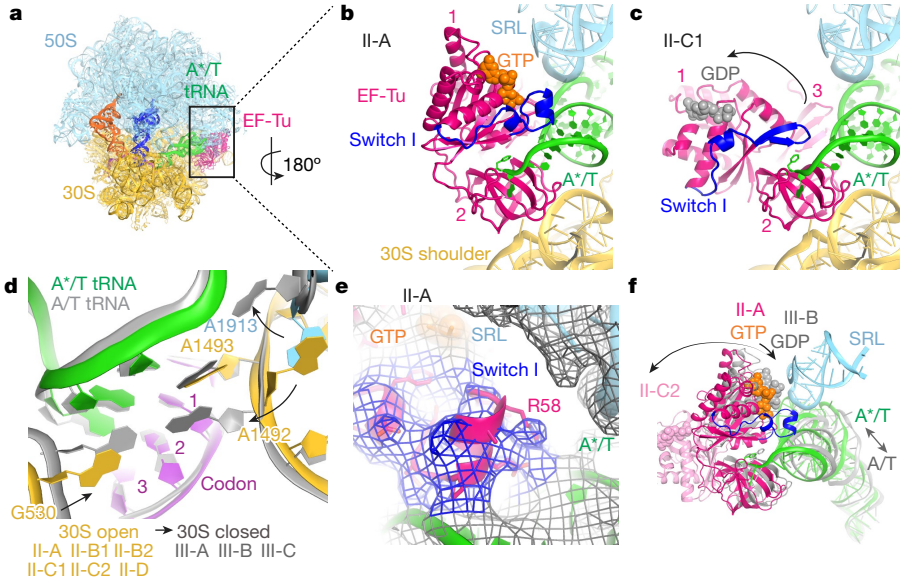

Fig. 2 | EF-Tu and ribosome rearrangements during mRNA decoding. **a**, Overview of the 70S ribosome bound with the ternary complex Phe-tRNA^{Phe}•EF-Tu•GTP (structure II-A). **b**, Compact EF-Tu•GTP with the ordered switch I region (blue) is separated from the SRL (cyan) on the ribosome with the open 30S conformation (structure II-A). **c**, Extended EF-Tu with domain 1 separated from tRNA (arrow) and with a reorganized switch I region (structure II-C1). **d**, Rearrangements in the decoding centre are coupled with 30S domain closure (shoulder shift) in the presence of EF-Tu. Structures II-A (coloured) and III-B (grey) are shown. **e**, Cryo-EM density showing EF-Tu with an ordered switch I region in the open 30S state (structure II-A). **f**, GTP (orange spheres) is hydrolysed (small black arrow), as the decoding centre accepts the tRNA (grey arrow; closed 30S), bringing domain 1 to the SRL (cyan). The disordering and refolding of switch I (blue) and the movement of domain 1 away from tRNA (larger black arrow) occur as the tRNA continues sampling open (A*/T) and closed (A/T) 30S conformations. EF-Tu from structures II-A (magenta with switch I in blue), III-B (grey) and II-C2 (light pink) is shown along with tRNA from II-A (A*/T, green) and III-B (A/T, grey).

compact conformation (Fig. 2c, Extended Data Fig. 3g, h, j, k, o, r). Despite the dissociation of domain 1, the tRNA remains well ordered because it is held in place by domain 2 (Extended Data Fig. 3w). Third, in one map (II-D), weak density for domain 3 (amino acids 300–392) continues to bridge the elbow of tRNA and the L11 stalk (Extended Data Fig. 3i, l), but domains 1 and 2 are not resolved. This map suggests that the dynamic domains 1 and 2 have been released from the acceptor arm of the tRNA (Extended Data Fig. 3x). II-D is therefore consistent with a late EF-Tu-dissociation state and/or an early tRNA-accommodation state.

Notably, ribosomes with compact and extended forms of EF-Tu sample both open (II-A to II-D) and closed (III-A to III-C) 30S subunit

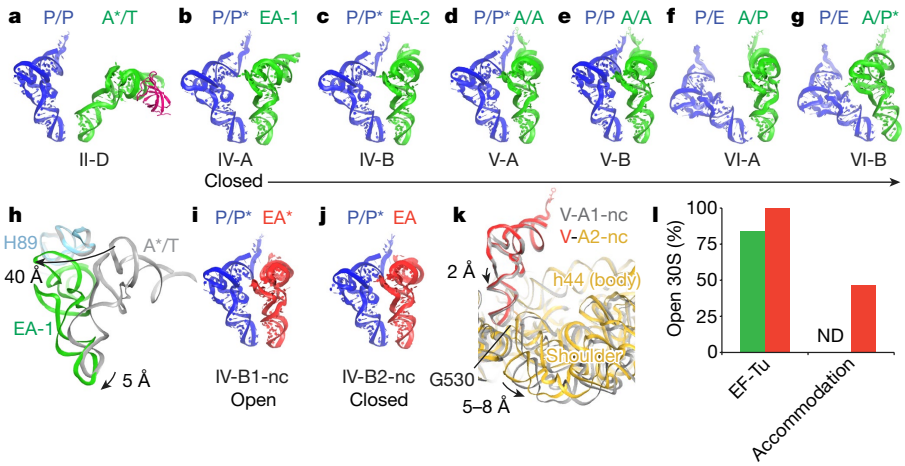

Fig. 3 | Differences between cognate and near-cognate tRNA accommodation. a–**g**, Cognate tRNA after EF-Tu release samples closed 30S conformations from accommodation to peptidyl transfer to pre-translocation states: **a**, EF-Tu domain 3 (magenta) is last to release from A*/T tRNA (green). **b**, Elbow-accommodated tRNA EA-1 in the ribosome with a partially rotated (approximately 2.5°) 30S subunit. **c**, Elbow-accommodated tRNA EA-2 is closer to the A site but the CCA end is not accommodated in the 50S A site. **d**, The CCA end of A tRNA is inserted into the PTC, as the 30S subunit is partially rotated (also Fig. 1f). **e**, Dipeptidyl-tRNA in the A site with the less-rotated 30S subunit (Extended Data Fig. 6b). **f**, **g**, Pre-translocation hybrid-state dipeptidyl-tRNA in the 70S with the fully rotated 30S subunit and different elbow positions of the A/P (**f**) and A/P* (**g**) tRNA (as defined in Supplementary Information). **h**, During accommodation, partial 30S rotation depresses tRNA and enables the tRNA to bypass H89. **i**, **j**, Near-cognate tRNA in elbow-accommodated states (IV-B1-nc, IV-B2-nc) samples open (**i**) and closed (**j**) 30S conformations. **k**, Near-cognate tRNA with accommodated CCA end samples open and closed 30S conformations, coupling the shoulder movement with tRNA destabilization. **l**, The 30S decoding centre samples open 30S conformations with near-cognate tRNA (red) in both EF-Tu-bound and accommodation structures (ND, not detected for cognate tRNA (green)).

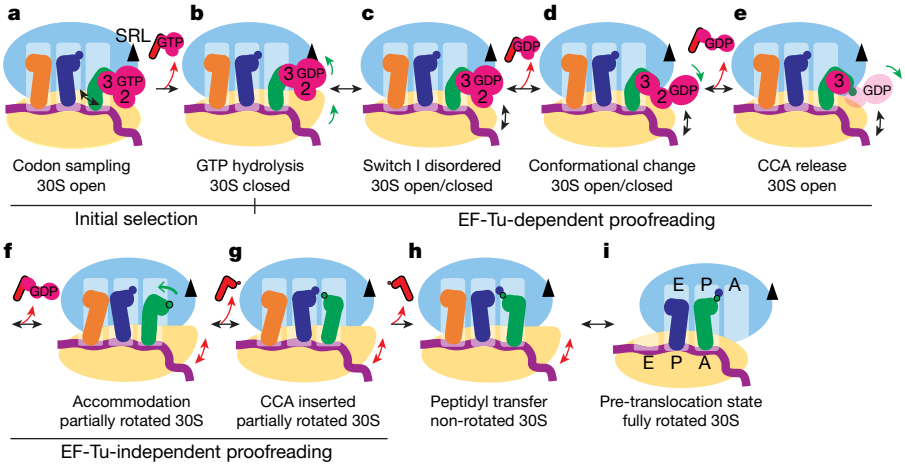

Fig. 4 | Schematic of mRNA decoding. a, **b**, Initial selection; **c**–**e**, EF-Tu-dependent proofreading; **f**, **g**, EF-Tu-independent proofreading; **h**, peptidyl transfer; **i**, pre-translocation. Black arrows denote events and conformational changes (EF-Tu rearrangements, 30S domain closure, and/or tRNA or EF-Tu dissociation) on both cognate (green tRNA) and near-cognate (red tRNA) decoding complexes. Green and red arrows denote events predominant for cognate and near-cognate complexes, respectively.

conformations (Fig. 2d, Extended Data Fig. 4b–e). The tRNA adopts kinked A*/T (A site/Ternary on open* 30S) and A/T (closed 30S) conformations, the anticodon stem–loops of which are respectively loosely and stably bound in the 30S decoding centre, consistent with our previous findings[5]. Rearrangement of the 30S subunit from an open to a closed conformation is coupled with movement of the decoding-centre nucleotide G530 towards A1492 and A1493 (Fig. 2d), as in structures II (open) and III (closed) in our previous work[5].

In all open 30S conformations with compact EF-Tu, the latter is separated from the SRL (II-A, II-B1 and II-B2). II-A has well-ordered switch I and II regions (Fig. 2e) and γ-phosphate is visible (Fig. 1e), consistent with functional states that precede GTP hydrolysis or phosphate release[24]. II-B1 and II-B2 have disordered switch I regions (Extended Data Fig. 3e, f), consistent with GDP being bound to compact EF-Tu. II-C1 (Fig. 2c) and II-C2 have extended EF-Tu conformations (Extended Data Fig. 3g, h), which resemble isolated EF-Tu•GDP[25], on the path to EF-Tu dissociation.

In the closed 30S conformations, compact EF-Tu is closer to the SRL. In III-A—in which the extent of domain closure appears to be intermediate—EF-Tu switch regions I and II are ordered, and EF-Tu tilts relative to the SRL (Extended Data Fig. 3m, p, y). The second, more-populated state III-B has a fully closed 30S subunit and disordered switch I and II regions, representing a GDP-bound state after GTP hydrolysis[13,29,30] (Fig. 2f, Extended Data Fig. 3n, q, y). Observation of compact EF-Tu in II-A and III-A is consistent with EF-Tu being separated from the SRL before GTP hydrolysis[5]. Structure III-B confirms that docking at the SRL, induced by the 30S closure, results in rapid GTP hydrolysis[27,31–35]. By contrast, III-C—in which the 30S is closed—contains extended EF-Tu (Extended Data Fig. 3o, r). The observation of extended EF-Tu in GDP states in both the open (II-C1 and II-C2) and the closed (III-C) 30S conformations indicates continuous 30S sampling after GTP hydrolysis (Extended Data Fig. 3g, h, o).

Our data are consistent with the following model for EF-Tu rearrangement (Fig. 4a–e). The ternary complex of aa-tRNA•EF-Tu•GTP initially binds the ribosome at the open-30S shoulder via EF-Tu, while tRNA samples the decoding centre. Upon codon recognition, G530 (at the 30S shoulder) and A1492 (at the 30S body) rearrange, shifting the 30S shoulder and bringing EF-Tu closer to the SRL (Fig. 2b, d). In the closed 30S conformation, EF-Tu docks at the SRL (Fig. 2f). The phosphate of A2662 of the SRL positions the conserved catalytic residue H84 of EF-Tu for GTP hydrolysis[5,27]. GTP hydrolysis and phosphate release destabilize the switch regions of EF-Tu because they no longer interact with γ-phosphate[13,36]. When the switch regions refold, the β-hairpin conformation of switch I[25] (Fig. 2c, Extended Data Fig. 3j) becomes sterically incompatible with binding to tRNA, so GTPase domain 1 dissociates from aa-tRNA and the SRL. Domain 2 then dissociates from the CCA-end of aa-tRNA. Domain 3, which may be partially stabilized by the N terminus of L11 and L7/L12 (Methods, Extended Data Fig. 3s–v), leaves last. The sequence of EF-Tu domain rearrangements is consistent with structural-dynamics simulations[21], and suggests that EF-Tu dissociation is unlikely to contribute to tRNA accommodation by a power-stroke-like mechanism[14].

As EF-Tu changes conformation, the 30S ribosomal subunit continues sampling the open conformation, wherein the decoding centre loosens its 'grip' on the codon–anticodon helix. The open 30S conformation is also observed in the absence of A-site tRNA, whereas the closed 30S conformation requires a bound anticodon stem–loop[37–39]. Thus, the aa-tRNA•EF-Tu complex may dissociate from the ribosome with an open 30S conformation in either GTP- or GDP-bound states—consistent with biochemical studies that have proposed EF-Tu-dependent proofreading[20].

30S locks and rotates as tRNA accommodates

When EF-Tu dissociates, the aa-tRNA arm must traverse 80 Å through the intersubunit space to accommodate into the PTC. Protrusions from the 50S subunit, however, form a narrow space for tRNA accommodation[40,41], and molecular-dynamics simulations have shown that 23S rRNA helices—most notably H89 (residues 2454–2498) and the A loop (H92)—occlude the tRNA path[15]. Our data reveal accommodation-like states (IV-A and IV-B) (Fig. 3, Extended Data Fig. 5c–f), which suggest that rotation of 30S and movement of the A-site finger (ASF) enable the tRNA to bypass the occlusions. Notably, the small subunit is closed in each accommodation state (Extended Data Fig. 4f). This indicates that EF-Tu dissociation substantially reduces the 30S opening dynamics with cognate tRNA, thereby 'locking' the tRNA into the decoding centre.

Four representative structures differ in the positions of the tRNA relative to the A site (Fig. 3a–d, Extended Data Fig. 5a–h): A*/T tRNA upon EF-Tu release (II-D); elbow-accommodated tRNA 1, close to A/T tRNA (EA-1 in IV-A); elbow-accommodated tRNA 2, close to the accommodated A/A tRNA (EA-2 in IV-B); and the CCA-accommodated A/A tRNA (V-A). In II-D, the elbow of A*/T tRNA interacts with the L11 stalk—as

described previously[5]—and the observation of weak density for EF-Tu domain 3 concurs with EF-Tu dissociation before tRNA accommodation (Fig. 3a, Extended Data Fig. 3i, l). In the EA-1 pre-accommodation state (Fig. 3b), the elbow of tRNA (at the backbone of C56) is shifted deeper into the ribosome—by around 40 Å—to interact with the long 50S hairpin loop that forms the ASF (nucleotides 863–915 of helix 38, 23S rRNA) (Fig. 3h). The acceptor arm of EA-1 (at the backbone of A73) lies around 30 Å from the A*/T state and around 35 Å from the 50S A site. The 3′ terminal strand of EA-1 points at C2559 of H92, whereas the middle of the acceptor arm (at A64) is held in place by H89 via RNA backbone–backbone packing (Fig. 3h, Extended Data Fig. 5c, d). EA-2 tRNA has bypassed H89, the CCA end is disordered, and the acceptor arm is approximately 7 Å from the position of A/A tRNA (measured at A73). Here, the acceptor arm is held in place near C2556 of H92 (Extended Data Fig. 5e, f). Both EA-1 and EA-2 are therefore transiently stabilized by interactions of the acceptor arm with different regions of H92.

In accommodation states IV-A and IV-B, the ribosome is rearranged relative to EF-Tu-bound states, enabling the tRNA to bypass the 23S rRNA obstacles and orient for CCA accommodation (Fig. 3b, c, h, Extended Data Fig. 5a, c). First, the closed 30S subunit of pre-accommodation ribosomes is rotated by approximately 2.5°. This 'partial accommodation rotation' (less than 9° observed in tRNA–mRNA translocation[2,42,43]) depresses the 30S A-site (at nucleotide 35 of tRNA) by around 5 Å relative to H89, enabling the tRNA to pass under H89 (Fig. 3h). The abundance of partially rotated ribosomes decreases over time, indicating that partial rotation occurs at intermediate stages of the elongation event (Extended Data Fig. 6c). Second, the ASF moves by more than 10 Å to bind the tRNA elbow and stabilize the elbow-accommodated tRNAs (Extended Data Fig. 7i). This interaction confines the conformational dynamics of tRNA to enable the insertion of CCA into the PTC.

Peptidyl transfer and pre-translocation

Four major states (V-A, V-B, VI-A and VI-B) suggest the progress of the peptidyl transfer reaction (Fig. 3d–g, Extended Data Fig. 6a, b, d–g; see discussion in Supplementary Information). In brief, V-A shows a partial rotation of the 30S subunit (similar to that in accommodation structures IV-A and IV-B); the reversal of which appears to align aminoacyl-tRNAs in the PTC for peptidyl transfer to occur as in V-B (Extended Data Fig. 6a, b). The ensuing peptidyl transfer and E-tRNA release enable a large, spontaneous rotation of the 30S subunit, resulting in formation of the canonical pre-translocation A/P and P/E tRNA hybrid states (VI-A) and elbow-shifted A/P* and P/E tRNAs (VI-B) (Figs. 1g, 3f, g), consistent with the results of many biochemical studies (reviewed in refs. [2,43]). Partial E-site occupancy by non-cognate tRNA in the structures preceding VI-A and VI-B suggests no correlation between the occupancies of the E and A sites in the decoding, accommodation or peptidyl-transfer states (Methods, Extended Data Fig. 6j–m).

Near-cognate tRNA samples open 30S without EF-Tu

To understand the structural basis of tRNA selection, we repeated our cryo-EM analysis for a near-cognate complex formed with Phe-tRNA^{Phe} and an mRNA carrying a leucine codon (**C**UC) to create an A–C mismatch at the first codon position. Sixteen maps suggest an elongation trajectory that is similar overall to that of the cognate complex (Extended Data Fig. 2c, Supplementary Information). We focus on differences in particle distributions and structures that provide insights into the decoding mechanism. Although we used buffer conditions to maximize rare miscoding events (refs. [20,44] and Methods), the distribution of particles in substrate, intermediate and product states indicates that elongation remained less efficient than with the cognate tRNA. Near-cognate ribosomes with an empty A site (substrates) were twofold more abundant, whereas the A-tRNA-bound (product) ribosomes were threefold less abundant in comparison with the cognate complex (Extended Data Fig. 7a). Moreover, the near-cognate complex was depleted of GDP-bound EF-Tu (compact with disordered switch I or extended conformations) (Extended Data Fig. 7b), which is consistent with less efficient GTP hydrolysis[45,46]. Indeed, EF-Tu-bound states predominantly sample the open 30S subunit (Fig. 3l)—similar to findings using GDPCP[5] (5'-guanosyl-β,γ-methylene-triphosphate, a non-hydrolysable GTP analogue)—indicating that anticodon stabilization, shoulder movement and EF-Tu docking at the SRL are less frequent than for the cognate ternary complex.

The most evident structural difference between near-cognate and cognate elongation complexes is in the accommodation states. After dissociation of EF-Tu, the accommodation EA intermediates with near-cognate tRNA continue to sample the open 30S conformation (IV-B1-nc) (Fig. 3i, l, Extended Data Fig. 5i–j), in contrast to cognate tRNA bound exclusively to the closed 30S subunit (Fig. 3l, Extended Data Fig. 4). Moreover, compared with the cognate EA tRNAs, the elbows of the near-cognate EA tRNAs contact the ASF more deeply (Extended Data Fig. 7j), and density maps suggest a dynamic anticodon stem–loop in the 30S A site (Extended Data Fig. 5i–j). When CCA is accommodated in the A site, a subset of near-cognate states also has an open 30S conformation (V-A1-nc, Fig. 3k, Extended Data Figs. 4j, 7e; and V-B1-nc, Extended Data Fig. 7g) and a disordered phenylalanine moiety, suggesting poor positioning of the substrate (Fig. 4k). A single mismatch therefore perturbs the accommodation pathway of near-cognate tRNA. Sampling of the open 30S conformation is consistent with release of near-cognate tRNA during both initial selection (EF-Tu-bound) and accommodation, the latter step constituting EF-Tu-independent proofreading. Structural obstacles, including H89 and H92, are likely to facilitate tRNA dissociation during the rotation and opening of the 30S subunit.

The mechanism of proofreading

Our structural analyses reveal that initial selection and proofreading—which were long thought to be biochemically separate events—are intertwined into a continuous process of mRNA decoding (Fig. 4). Although GTP hydrolysis triggers the release of EF-Tu, our data are consistent with the hypothesis that proofreading occurs both before and after EF-Tu dissociation, suggesting a revised mechanistic role for EF-Tu•GTP (Supplementary Information, see section 'Conformational proofreading'). All three decoding steps——initial selection (before GTP hydrolysis) (Fig. 4a, b), EF-Tu-dependent proofreading (after GTP hydrolysis) (Fig. 4c–e) and EF-Tu-independent proofreading (after EF-Tu release) (Fig. 4f, g)——rely on conceptually similar structural mechanisms. They involve the 'locking/unlocking' dynamics of the 30S decoding centre, and steric hindrances induced by EF-Tu (during initial selection and EF-Tu-dependent proofreading) or by the protruding 50S rRNA (during accommodation). EF-Tu continuously destabilizes closure of the 30S subunit in both cognate and near-cognate complexes, before and after GTP hydrolysis. Destabilization of the closed 30S conformation probably arises from the strained conformation of the kinked A/T tRNA, the anticodon stem–loop of which samples the decoding centre while the CCA end remains pinned by EF-Tu at the 30S shoulder (Fig. 2a). Near-cognate tRNA is prone to dissociation from open 30S states during both initial selection (with EF-Tu•GTP) and proofreading (with EF-Tu•GDP)[20] because the mismatched mRNA–tRNA codon–anticodon helix is unstable in the decoding centre. Cognate tRNA is retained by stabilizing interactions with decoding-centre nucleotides G530, A1492 and A1493 even in open 30S states[5] (Fig. 2d).

After GTP hydrolysis and EF-Tu dissociation (Fig. 4a–e), the EF-Tu-independent stage of proofreading begins. At this stage, tRNA relaxes on its way towards the 50S A site (Fig. 4f). The ribosome—with 30S in a closed state—appears to be 'committed' to accommodation of cognate tRNA, the ASL of which is stably locked in the decoding centre owing to tRNA conformational relaxation, consistent with rapid

accommodation and peptide-bond formation[31,47]. Partial rotation of the 30S subunit enables the tRNA to bypass rRNA protrusions, and probably aids proofreading by delaying peptide-bond formation until the 30S rotation is reversed (Fig. 4g, h). By contrast, ribosomes with an accommodating near-cognate tRNA continue to sample the 30S in open states (Fig. 4f, g), which destabilize the near-cognate tRNA at two major points of contact: the decoding centre and the ASF. Furthermore, 50S protrusions—including H89—probably destabilize the accommodating tRNA. Continuous sampling of open 30S restricts the entry of near-cognate tRNA into the PTC, consistent with tRNA rejection after EF-Tu release[11] and reduced rates for accommodation and peptide-bond formation[11,20]. The minimization of miscoding events therefore results from continuous verification of tRNA throughout the A*/T→EA→A/A trajectory. The universally conserved decoding centre and small-subunit dynamics therefore dictate high translation fidelity.

Cryo-EM enabled us to resolve many transient intermediates in the course of a GTP-catalysed reaction without the use of inhibitors. Recent advances in cryo-EM make it possible to rapidly apply samples to electron microscopy grids[48,49] and to deconvolute heterogeneous ensembles of numerous structures at near-atomic resolution[16,50,51]. Together, these studies emphasize that high-resolution time-resolved cryo-EM—as a structural biochemistry technique—could become the method of choice for visualizing complex biochemical pathways without inhibitors.

Online content

Any methods, additional references, Nature Research reporting summaries, source data, extended data, supplementary information, acknowledgements, peer review information; details of author contributions and competing interests; and statements of data and code availability are available at https://doi.org/10.1038/s41586-020-2447-x.

1. Hopfield, J. J. Kinetic proofreading: a new mechanism for reducing errors in biosynthetic processes requiring high specificity. *Proc. Natl Acad. Sci. USA* **71**, 4135–4139 (1974).
2. Voorhees, R. M. & Ramakrishnan, V. Structural basis of the translational elongation cycle. *Annu. Rev. Biochem.* **82**, 203–236 (2013).
3. Pavlov, M. Y. & Ehrenberg, M. Substrate-induced formation of ribosomal decoding center for accurate and rapid genetic code translation. *Annu. Rev. Biophys.* **47**, 525–548 (2018).
4. Rodnina, M. V., Fischer, N., Maracci, C. & Stark, H. Ribosome dynamics during decoding. *Phil. Trans. R. Soc. Lond. B* **372**, 20160182 (2017).
5. Loveland, A. B., Demo, G., Grigorieff, N. & Korostelev, A. A. Ensemble cryo-EM elucidates the mechanism of translation fidelity. *Nature* **546**, 113–117 (2017).
6. Fislage, M. et al. Cryo-EM shows stages of initial codon selection on the ribosome by aa-tRNA in ternary complex with GTP and the GTPase-deficient EF-Tu^{H84A}. *Nucleic Acids Res.* **46**, 5861–5874 (2018).
7. Moazed, D. & Noller, H. F. Intermediate states in the movement of transfer RNA in the ribosome. *Nature* **342**, 142–148 (1989).
8. Yusupov, M. M. et al. Crystal structure of the ribosome at 5.5 Å resolution. *Science* **292**, 883–896 (2001).
9. Stark, H. et al. Visualization of elongation factor Tu on the *Escherichia coli* ribosome. *Nature* **389**, 403–406 (1997).
10. Ehrenberg, M. & Blomberg, C. Thermodynamic constraints on kinetic proofreading in biosynthetic pathways. *Biophys. J.* **31**, 333–358 (1980).
11. Pape, T., Wintermeyer, W. & Rodnina, M. Induced fit in initial selection and proofreading of aminoacyl-tRNA on the ribosome. *EMBO J.* **18**, 3800–3807 (1999).
12. Fischer, N. et al. Structure of the *E. coli* ribosome–EF-Tu complex at <3 Å resolution by Cs-corrected cryo-EM. *Nature* **520**, 567–570 (2015).
13. Schmeing, T. M. et al. The crystal structure of the ribosome bound to EF-Tu and aminoacyl-tRNA. *Science* **326**, 688–694 (2009).
14. Noel, J. K. & Whitford, P. C. How EF-Tu can contribute to efficient proofreading of aa-tRNA by the ribosome. *Nat. Commun.* **7**, 13314 (2016).
15. Sanbonmatsu, K. Y., Joseph, S. & Tung, C. S. Simulating movement of tRNA into the ribosome during decoding. *Proc. Natl Acad. Sci. USA* **102**, 15854–15859 (2005).
16. Abeyrathne, P. D., Koh, C. S., Grant, T., Grigorieff, N. & Korostelev, A. A. Ensemble cryo-EM uncovers inchworm-like translocation of a viral IRES through the ribosome. *eLife* **5**, e14874 (2016).
17. Thompson, R. C., Dix, D. B., Gerson, R. B. & Karim, A. M. A GTPase reaction accompanying the rejection of Leu-tRNA$_2$ by UUU-programmed ribosomes. *J. Biol. Chem.* **256**, 81–86 (1981).
18. Dunkle, J. A. et al. Structures of the bacterial ribosome in classical and hybrid states of tRNA binding. *Science* **332**, 981–984 (2011).
19. Korostelev, A., Trakhanov, S., Laurberg, M. & Noller, H. F. Crystal structure of a 70S ribosome–tRNA complex reveals functional interactions and rearrangements. *Cell* **126**, 1065–1077 (2006).
20. Ieong, K. W., Uzun, Ü., Selmer, M. & Ehrenberg, M. Two proofreading steps amplify the accuracy of genetic code translation. *Proc. Natl Acad. Sci. USA* **113**, 13744–13749 (2016).
21. Yang, H., Perrier, J. & Whitford, P. C. Disorder guides domain rearrangement in elongation factor Tu. *Proteins* **86**, 1037–1046 (2018).
22. Kothe, U. & Rodnina, M. V. Delayed release of inorganic phosphate from elongation factor Tu following GTP hydrolysis on the ribosome. *Biochemistry* **45**, 12767–12774 (2006).
23. Kavaliauskas, D. et al. Structural dynamics of translation elongation factor Tu during aa-tRNA delivery to the ribosome. *Nucleic Acids Res.* **46**, 8651–8661 (2018).
24. Berchtold, H. et al. Crystal structure of active elongation factor Tu reveals major domain rearrangements. *Nature* **365**, 126–132 (1993).
25. Polekhina, G. et al. Helix unwinding in the effector region of elongation factor EF-Tu-GDP. *Structure* **4**, 1141–1151 (1996).
26. Kjeldgaard, M., Nissen, P., Thirup, S. & Nyborg, J. The crystal structure of elongation factor EF-Tu from *Thermus aquaticus* in the GTP conformation. *Structure* **1**, 35–50 (1993).
27. Voorhees, R. M., Schmeing, T. M., Kelley, A. C. & Ramakrishnan, V. The mechanism for activation of GTP hydrolysis on the ribosome. *Science* **330**, 835–838 (2010).
28. Kothe, U., Wieden, H. J., Mohr, D. & Rodnina, M. V. Interaction of helix D of elongation factor Tu with helices 4 and 5 of protein L7/12 on the ribosome. *J. Mol. Biol.* **336**, 1011–1021 (2004).
29. Schuette, J. C. et al. GTPase activation of elongation factor EF-Tu by the ribosome during decoding. *EMBO J.* **28**, 755–765 (2009).
30. Villa, E. et al. Ribosome-induced changes in elongation factor Tu conformation control GTP hydrolysis. *Proc. Natl Acad. Sci. USA* **106**, 1063–1068 (2009).
31. Pape, T., Wintermeyer, W. & Rodnina, M. V. Complete kinetic mechanism of elongation factor Tu-dependent binding of aminoacyl-tRNA to the A site of the *E. coli* ribosome. *EMBO J.* **17**, 7490–7497 (1998).
32. Hausner, T. P., Atmadja, J. & Nierhaus, K. H. Evidence that the G2661 region of 23S rRNA is located at the ribosomal binding sites of both elongation factors. *Biochimie* **69**, 911–923 (1987).
33. Moazed, D., Robertson, J. M. & Noller, H. F. Interaction of elongation factors EF-G and EF-Tu with a conserved loop in 23S RNA. *Nature* **334**, 362–364 (1988).
34. Daviter, T., Wieden, H. J. & Rodnina, M. V. Essential role of histidine 84 in elongation factor Tu for the chemical step of GTP hydrolysis on the ribosome. *J. Mol. Biol.* **332**, 689–699 (2003).
35. Maracci, C., Peske, F., Dannies, E., Pohl, C. & Rodnina, M. V. Ribosome-induced tuning of GTP hydrolysis by a translational GTPase. *Proc. Natl Acad. Sci. USA* **111**, 14418–14423 (2014).
36. Koripella, R. K. et al. A conserved histidine in switch-II of EF-G moderates release of inorganic phosphate. *Sci. Rep.* **5**, 12970 (2015).
37. Ogle, J. M. et al. Recognition of cognate transfer RNA by the 30S ribosomal subunit. *Science* **292**, 897–902 (2001).
38. Ogle, J. M. & Ramakrishnan, V. Structural insights into translational fidelity. *Annu. Rev. Biochem.* **74**, 129–177 (2005).
39. Demeshkina, N., Jenner, L., Westhof, E., Yusupov, M. & Yusupova, G. A new understanding of the decoding principle on the ribosome. *Nature* **484**, 256–259 (2012).
40. Whitford, P. C. et al. Accommodation of aminoacyl-tRNA into the ribosome involves reversible excursions along multiple pathways. *RNA* **16**, 1196–1204 (2010).
41. Jenner, L., Demeshkina, N., Yusupova, G. & Yusupov, M. Structural rearrangements of the ribosome at the tRNA proofreading step. *Nat. Struct. Mol. Biol.* **17**, 1072–1078 (2010).
42. Frank, J. & Agrawal, R. K. A ratchet-like inter-subunit reorganization of the ribosome during translocation. *Nature* **406**, 318–322 (2000).
43. Noller, H. F., Lancaster, L., Zhou, J. & Mohan, S. The ribosome moves: RNA mechanics and translocation. *Nat. Struct. Mol. Biol.* **24**, 1021–1027 (2017).
44. Zhang, J., Pavlov, M. Y. & Ehrenberg, M. Accuracy of genetic code translation and its orthogonal corruption by aminoglycosides and Mg^{2+} ions. *Nucleic Acids Res.* **46**, 1362–1374 (2018).
45. Zhang, J., Ieong, K. W., Johansson, M. & Ehrenberg, M. Accuracy of initial codon selection by aminoacyl-tRNAs on the mRNA-programmed bacterial ribosome. *Proc. Natl Acad. Sci. USA* **112**, 9602–9607 (2015).
46. Gromadski, K. B. & Rodnina, M. V. Kinetic determinants of high-fidelity tRNA discrimination on the ribosome. *Mol. Cell* **13**, 191–200 (2004).
47. Johansson, M., Bouakaz, E., Lovmar, M. & Ehrenberg, M. The kinetics of ribosomal peptidyl transfer revisited. *Mol. Cell* **30**, 589–598 (2008).
48. Fu, Z. et al. Key intermediates in ribosome recycling visualized by time-resolved cryoelectron microscopy. *Structure* **24**, 2092–2101 (2016).
49. Kaledhonkar, S. et al. Late steps in bacterial translation initiation visualized using time-resolved cryo-EM. *Nature* **570**, 400–404 (2019).
50. Nikolay, R. et al. Structural visualization of the formation and activation of the 50S ribosomal subunit during in vitro reconstitution. *Mol. Cell* **70**, 881–893.e3 (2018).
51. Graf, M. et al. Visualization of translation termination intermediates trapped by the Apidaecin 137 peptide during RF3-mediated recycling of RF1. *Nat. Commun.* **9**, 3053 (2018).

Publisher's note Springer Nature remains neutral with regard to jurisdictional claims in published maps and institutional affiliations.

© The Author(s), under exclusive licence to Springer Nature Limited 2020

Methods

We performed ensemble cryo-EM[16] of EF-Tu•GTP-catalysed delivery of cognate aa-tRNA at several time points. We incubated Phe-tRNA^{Phe}•EF-Tu•GTP ternary complex with *Escherichia coli* 70S•fMet-tRNA^{fMet} programmed with mRNA carrying the initiation fMet (AUG) codon in the P site and a Phe (UUC) codon in the A site (Fig. 1a). The reactions progressed on ice (to slow the reactions), were applied to cryo-EM grids, and were rapidly plunged into liquid ethane to stop their progress at different times (Fig. 1c, Methods). Datasets were collected for time points informed by a biochemical time course of the EF-Tu•GTP-catalysed reaction under similar conditions[17].

Preparation and freezing of tRNA delivery complexes on cryo-EM grids

Ribosomal subunits (30S and 50S) were prepared from MRE600 *E. coli* as described[52] and stored in buffer A (20 mM Tris, pH 7, 10.5 mM $MgCl_2$, 100 mM NH_4Cl, 0.5 mM EDTA, 6 mM β-mercaptoethanol) at −80 °C. mRNA containing the Shine–Dalgarno sequence and a linker to place the AUG codon in the P site and the Phe codon (cognate complex) or Leu codon (near-cognate complex) in the A site was synthesized by Integrated DNA Technologies. The cognate complex mRNA was GGC AAG GAG GUA AAA **AUG UUC** AAA AAA, whereas the near-cognate complex mRNA was GGC AAG GAG GUA AAA **AUG CUC** AAA AAA.

Components of the ternary complex were prepared as follows. *E. coli* EF-Tu was prepared as previously described[5,53]. GTP was purchased from Roche. tRNA^{Phe} and tRNA^{fMet} were purchased from Chemblock. Cellular enzyme extract (S-100) was used for tRNA aminoacylation and was prepared from MRE600 *E. coli* as described[53]. In brief, 2 l of MRE600 *E. coli* culture in LB was collected in log phase (optical density at 600 nm (OD_{600}) 0.6) yielding approximately 5 g of cell pellet. The pellet was resuspended in 20 ml of S-100 buffer (10 mM Tris, pH 7, 10 mM $MgCl_2$, 30 mM NH_4Cl, 6 mM β-mercaptoethanol) and the cells were lysed using a Microfluidics M-110P cell disruptor. The lysate was cleared by centrifugation at 15,000 rpm for 15 min at 4 °C (JA-20 rotor, Beckman). Ribosomes were pelleted out of the cleared lysate using ultracentrifugation in a Ti-70 rotor (Beckman) at 60,000 rpm, for 2 h at 4 °C. Next, 2.5 g of DEAE cellulose (Sigma Aldrich) was equilibrated and washed three times with ice cold S-100 buffer. Following the ultracentrifugation, the top 80% of the supernatant was transferred to the DEAE cellulose and allowed to mix for 30 min at 4 °C. The DEAE cellulose was separated from solution by centrifugation in a table-top centrifuge at 5,000 rpm for 5 min at 4 °C and the supernatant was removed. DEAE cellulose was washed with 40 ml of S-100 buffer for 30 min at 4 °C. The DEAE cellulose beads were isolated and mixed with 10 ml of S-100 elution buffer (10 mM Tris, pH 7, 10 mM $MgCl_2$, 250 mM NH_4Cl, 6 mM β-mercaptoethanol) for 30 min at 4 °C. After centrifuging as before to separate the DEAE cellulose and supernatant, the supernatant was retained and used as the purified S-100 extract. tRNA^{Phe} and tRNA^{fMet} were charged using the S-100 extract supplemented with 0.1 mM phenylalanine or methionine, respectively, exactly as described previously[53]. The methionine was formylated by including neutralized N10-formyl-tetrahydrofolate in the reaction[53]. Aminoacylation and formylation of tRNA were confirmed using acid gel electrophoresis[54], as shown in Extended Data Fig. 5q, r.

The 70S and ternary complexes were prepared as follows. Heat-activated (42 °C, 5 min) 30S ribosomal subunits (3 μM) were mixed with 50S ribosomal subunits (3 μM) and with cognate or near-cognate complex mRNA (15 μM) (all final concentrations) in reaction buffer (20 mM HEPES·KOH, pH 7.5, 20 mM magnesium chloride, 150 mM ammonium chloride, 2 mM spermidine, 0.1 mM spermine) for 30 min at 37 °C. A 2.25-fold molar excess of fMet-tRNA^{fMet} was added to the ribosomal subunits and incubated for 5 min at 37 °C. The 70S•mRNA•fMet-tRNA^{fMet} complexes were diluted to 0.5 μM with reaction buffer and held on ice. Concurrently, the ternary complex of Phe-tRNA^{Phe}•EF-Tu•GTP was prepared as follows. 1.5 μM EF-Tu was pre-incubated with 1 mM GTP in reaction buffer for 5 min at 37 °C and then was supplemented with 1.5 μM Phe-tRNA^{Phe} (all final concentrations). After an additional minute at 37 °C, the ternary complex was also kept on ice until plunging.

C-flat 1.2-1.3 (Protochips) holey-carbon grids coated with a thin layer of carbon (17 s, 29 s, 120 s cognate and 30 s near-cognate datasets) or Ultrathin Carbon Film on Lacey Carbon Support Film (Ted Pella) (0 s and 1800 s cognate datasets) grids were glow discharged with 20 mA current with negative polarity for 45–60 s in a PELCO easiGlow glow discharge unit. A Vitrobot Mark IV was pre-equilibrated to around 4.5 °C and 100% humidity for 1 h before plunging. Pipettes, tips, tubes and forceps were equilibrated on ice for 30 min before the beginning of the plunging procedure and kept on ice when not in use during the procedure. For each grid, 1.5 μl of 70S•mRNA•fMet-tRNA^{fMet} was mixed with 1.5 μl of ternary complex with ice-chilled tips and in an ice-chilled tube. Approximately 10 s before the desired time point, the reaction was transferred from the tube in an ice-chilled tip into the Vitrobot chamber, quickly applied to a chilled holey-carbon grid, and then blotted for 4 s before plunging into liquid-nitrogen-cooled liquid ethane. The time point when the grid hit the ethane was noted as the reaction duration. The cognate data presented are from grids prepared from the same half reactions and plunged at 17 s, 29 s and 120 s within 30 min of each other. The near-cognate data are from a grid prepared at the same plunging session, using the same ternary complex preparation with ribosomes programmed with the Leu-encoding mRNA. The 0 s and 1,800 s data were prepared using the same procedure, with buffer used instead of ternary complex for the 0 s time point. The final reactions on the grids had the following concentrations: 250 nM 50S; 250 nM 30S; 1.25 μM mRNA; 560 nM fMet-tRNA^{fMet}; 0.75 μM EF-Tu; 500 μM GTP and 0.75 μM Phe-tRNA^{Phe}.

Electron microscopy

Data for the cognate tRNA delivery complexes at 0, 17, 29, 120 and 1,800 s and near-cognate complex at 30 s were collected on a Titan Krios electron microscope (FEI) operating at 300 kV and equipped with a Gatan Image Filter (GIF) and a K2 Summit direct electron detector (Gatan) targeting 0.3 to 2.0-μm underfocus. For the cognate, 29-s time point, a dataset of 678,268 particles from 3,218 movies was collected automatically using SerialEM[55]. Similarly, for the cognate complex, data were collected as follows: 0 s, 7,428 particles from 67 movies; 17 s, 375,869 particles from 1,640 movies; 120 s, 127,089 particles from 666 movies; and 1,800 s, 13,126 particles from 167 movies. For the near-cognate complex, one 30-s time point was similarly collected and included 565,412 particles from 2,508 movies. For each data collection, 35–36 frames per movie were collected at 1 $e^-/Å^2$ per frame for a total dose of 35–36 $e^-/Å^2$ on the sample. The super-resolution pixel size was 0.667 Å on the sample as calibrated from cross-correlation of the atomic model of Protein Data Bank (PDB) structures 5UYL or 5UYM[5] to the maps for structures II-A and III-B, respectively, using Chimera.

Image processing

Particles were extracted from aligned movie sums as follows. Movies were processed using IMOD[56] to decompress frames, apply the gain reference, and to correct for image drift yielding image sums with pixel size of 1.333 Å. CTFFIND4[57] was used to determine defocus values. Particles were automatically picked from 5× -binned images using Signature[58] with a ribosome reference (18 representative reprojections of the Electron Microscopy Data Bank (EMDB) map 1003[59]). Then, 288 × 288-pixel boxes with particles were extracted from motion-corrected images, and assembled into stacks in EMAN2[60]. To speed up processing, 2×-binned and 4×-binned image stacks were prepared using resample.exe, which is part of the Frealign distribution[61].

Optimization of grid preparation for time-resolved cryo-EM

The conditions for complex preparation, grid freezing and data collection were optimized to yield the conditions described in the above sections. Using small datasets (10,000–50,000 particles) we tested different plunging approaches, including a manual plunger and CP3 (Gatan) operating in a cold room (Brandeis University Cryo-EM facility); Vitrobot Mark IV (UMass Medical School Cryo-EM core facility), different grid types (holey-carbon grids or carbon-coated holey-carbon grids), reaction duration (4 s to 60 s), temperature (up to 10 °C), reaction conditions (varying ternary complex to ribosome ratio and buffer composition) and dataset size. Datasets were collected on F20 or F30 electron microscopes at Brandeis University. The datasets were processed using the procedures described above and classified as described below but were modified to allow for the different microscopes and detectors used. We observed the following trends. The CP3 plunger allowed us to achieve fastest reaction times from mixing to plunging within 4 s, but suffered from poor temperature control and inconsistent grid quality owing to fast handling. We observed about 5% occupancy of EF-Tu and about 10% accommodated A-tRNA in these early experiments, and found that 15–30 s time points led to increased populations of intermediates. Use of holey-carbon or carbon-coated holey-carbon grids yielded approximately equivalent EF-Tu loading onto ribosomes after correcting for ribosome density (typically, 7 times higher concentrations of the 70S complexes were used for holey-carbon grids). Use of carbon-coated grids, however, yielded more consistent ice thickness and higher-resolution reconstructions.

To test whether EF-Tu occupancy estimation at different time points could be biased owing to the variation in dataset sizes, we analysed 10 smaller datasets (around 20,000 to around 50,000 particles) from reactions quenched at 20 to 30 s. Data classification consistently revealed EF-Tu at 10–20% occupancy, ruling out the bias.

Classifications

In parallel with the classification approach shown in Extended Data Figs. 1 and 2 and described in detail below, we performed over 100 classifications that differed by the number of classes (from 2 to 48), number of classification steps, masking approaches (3D mask and spherical focus mask in Frealign), mask positions and sizes (30S, A-site, A- and P-sites, PTC, L11 stalk, and so on) and resolution cutoffs (ranging from 12 Å to 4 Å). These classifications resulted in more than 1,000 maps, which generally reproduced the classes discussed in the main text. The classifications revealed different positions of the mobile parts of the ribosome, including the L1 and L11 stalks. We discovered additional features, which are consistent with elusive interactions between EF-Tu and a highly dynamic L7/L12 stalk, implicated in recruiting the ternary complex to the ribosome[28,62], as described in Supplementary Information and Extended Data Fig. 3s–v.

Distribution of states

Extensive maximum-likelihood classification of datasets at different time points was performed to identify the intermediates that might characterize substrate-like, EF-Tu-bound, accommodation, peptidyl transfer and pre-translocation sub-states (Fig. 1b). EF-Tu-bound particles were found at similar abundance at the early time points (up to 30 s) in smaller and large datasets, ruling out a bias in the classification and abundance estimation due to dataset size and clearly fell in the 120 s time point (see above). We observed no A/A, EA or A/P tRNA (product) states at the 0-s time point. The presence of these states upon addition of the ternary complex (at 17 s, 30 s and 120 s)—in which EF-Tu was present in excess over aa-tRNA—demonstrates that the decoding, accommodation, peptidyl-transfer and pre-translocation states result from interaction with the ternary complex and are not due to pre-bound or spontaneously re-binding tRNA in the initial 70S ribosome sample.

The extent of partial 30S subunit rotation—which is associated with tRNA accommodation upon EF-Tu release (Fig. 3h)—reduces with time (Extended Data Fig. 6c), consistent with accommodation being a slow and potentially rate-limiting step[31]. By contrast, ribosome populations within EF-Tu-bound states (structures II-A to II-C2 and III-A to III-C) at 17 and 120 s are similar to those at 29 s. This suggests that interconversions among EF-Tu-bound states occur with fast rates, and involve ribosomes that bind the ternary complex at earlier and later time points. At the later time points, EF-Tu-bound intermediates probably report on ribosomes that proceeded through multiple cycles of binding and dissociation of EF-Tu ternary complex, and/or dissociation of the accommodating tRNA. Similarly, the distribution of product states in non-rotated and rotated 70S conformations (structures V and VI) remain similar with respect to each other, consistent with fast interconversions observed by fluorescence resonance energy transfer (FRET) studies[63].

High-resolution classifications, map refinement and reconstruction

Frealign v.9.11 was used for most steps of refinement and reconstruction[61] (Extended Data Figs. 1, 2). Image stacks (4×-binned) were initially aligned to a ribosome reference[59] (EMDB map 1003) using three rounds of mode 3 (global search) alignment, including data in the resolution range from 300 Å to 20 Å. Next, the 2×-binned and later unbinned image stacks were successively aligned against the common reference using mode 1 (local refinement), including data up to a high-resolution limit of 6 Å (cognate 17 s, 29 s, 120 s; near-cognate 30 s) or 8 Å (cognate 0 s, 1,800 s). Subsequently, the refined parameters were used for classification of 4×-binned stacks into 8 classes (cognate 0 s, 17 s, 29 s, 1,800 s) or 20 classes (cognate 120 s or near-cognate 30 s) in 50 rounds using a spherical (50 Å radius) focus mask around EF-Tu and A/T tRNA, including resolutions from 300 Å to 12 Å during classification. This classification (classification 1) separated ribosomes in the classical and hybrid state from 50S subunits, and in each case (except 0 s and 1,800 s) included one class with density for EF-Tu.

Classification of cognate EF-Tu states. To find an optimal strategy to resolve distinct states of EF-Tu-containing particles, we compared individual classifications of the 17-s, 29-s and 120-s datasets against that of a combined stack of EF-Tu-containing particles (as described in the next paragraph). We independently classified EF-Tu-containing classes of the 17s-, 29-s and 120-s datasets, using a 3D mask around the 30S shoulder domain and then a 30 Å focus mask centred around EF-Tu, as described below. We also tested classifications with other masks encircling EF-Tu. These approaches and analyses of dozens of maps revealed that individual EF-Tu-containing states are structurally similar between these three datasets, revealing independently: the 30S domain closure, EF-Tu movements and domain rearrangements. This result suggested that similar structural states are sampled in the course of the reaction, and that we might be able to improve the resolution of the final maps by combining these data. Indeed, classifications of the combined datasets reproducibly improved the density for EF-Tu, and the average resolutions for EF-Tu-containing classes improved by 0.1–0.3 Å. Map improvements were confirmed by visual inspections of the densities originating from the 17-s, 29-s and the combined datasets.

The particles bound with EF-Tu in classification 1 of the cognate datasets were extracted using merge_classes.exe including particles with greater than 50% occupancy and scores greater than 0 (29,453 particles at 17 s, 47,421 particles at 29 s and 2,964 particles at 120 s). These stacks were appended and all 79,838 particles were processed together to increase the resolution of the final classes as described above. The joint stack was first aligned by running 3 rounds of mode 1 refinement including resolution from 300 Å to 8 Å during refinement. Next, the particles were separated into two classes using a 3D mask that included the shoulder domain of the 30S subunit to separate particles with an open 30S from those with the closed 30S conformation. Two new stacks were prepared and further subclassified into 4 (closed 30S)

or 6 classes (open 30S) using a small focus mask (30 Å) centred around EF-Tu using data up to 12 Å resolution for classification only (Extended Data Fig. 1b). After 50 rounds of classification, maps were prepared from the unbinned stack and used without further orientation refinement. Eight of these 10 classes were modelled and refined and are described in the text as structures II-A, II-B1, II-B2, II-C1, II-C2, III-A, III-B, and III-C. To obtain the best possible map of the EF-Tu release state (II-D), the open 30S particle stack was separated into 10 classes using a larger focus mask (60 Å) centred at EF-Tu. This classification separated out particles that were interacting with L11 and L7/L12 in different ways (Extended Data Fig. 3s–v), particles in which EF-Tu was close to other ribosomes (not shown), and a cleaner release intermediate state which was fit as state II-D.

Classification of accommodation and peptidyl transfer intermediates. Classical-state 70S classes (with non-rotated or partially rotated 30S) with either two tRNAs and a weak ASL in the A site or three well-ordered tRNAs from classification 1 were merged using merge_classes.exe including particles with greater than 50% occupancy and scores greater than 0 (201,764 particles) and were further subclassified into 24 classes using a 46 Å focus mask around the A and P sites of the 30S and 50S ribosomal subunits using data up to 12 Å resolution (Extended Data Fig. 1a). After 250 rounds of classification, 13 classes contained three tRNA, 3 classes were accommodation intermediates, 5 classes had empty A sites in the classical (4) or hybrid (1) conformation, and 3 classes were low resolution. The particles from the 13 classes with three tRNA were extracted using merge_classes.exe including particles with greater than 50% occupancy and scores of greater than 20 (83,981 particles) and separated into two classes using the same 46 Å focus mask, 50 rounds, and data to 12 Å. This classification yielded maps corresponding to models V-A and V-B. These classes were extracted for further exploratory subclassifications (see Supplementary Information) and were independently refined to improve map resolution. Particles belonging to the accommodation intermediate with the elbow at the ASF and a disordered acceptor arm were extracted using merge_classes.exe including particles with greater than 50% occupancy and scores greater than 0 (8,072 particles) and were separated into five classes using a 30-Å focus mask centred around the disordered acceptor arm using 50 rounds and data to 12 Å resolution. Two of these maps with the best features are modelled as states IV-A and IV-B.

Classification of hybrid states. The hybrid-state particles (with fully rotated 30S) from classification 1 were also extracted using merge_classes.exe including particles with greater than 25% occupancy and scores greater than 0 (141,604 particles) and were further subclassified into 8 classes using the same 50 Å focus mask as classification 1 (Extended Data Fig. 1a). After 50 rounds of classification, 2 classes contained two tRNAs (one dipeptidyl-tRNA in the A/P site and one deacylated tRNA in the P/E sites, with different positions of the A/P tRNA elbow) similar to states VI-A and VI-B. The six remaining classes contained one tRNA in the P/E conformation, and the class with the best-resolved features was modelled as class I-B. Limiting the hybrid-state particle stack to those particles with greater than 50% occupancy and scores of greater than 20 from classification 1 and repeating the classification yielded the product ribosome states exhibiting higher resolution features in the PTC, and ultimately these were modelled as states VI-A and VI-B.

Classification of the partially occupied E site. To investigate the occupancy of the E site, we used maximum likelihood classification of the 29-s particle substack within a 30-Å focus mask centred on the E-site. To this end, the substrate-like particles (non-rotated 70S with empty A site, 104,795 particles), EF-Tu-containing particles with the domain-open 30S (24,120 particles), EF-Tu-containing particles with the domain-closed 30S (15,216 particles), elbow-accommodation particles (8,072 particles) and peptidyl-transfer-like particles (83,981 particles) (see Extended Data Fig. 1a) were separately classified into 8 classes for 50 rounds, using data up to 12 Å resolution. In each case, 1–2 classes contained no E-tRNA and 0–1 classes contained weak tRNA-elbow-like density at the L1 stalk with no density for the acceptor arm and ASL. The population of the weak/vacant E-site is constant (around 20–25%) among the substrate-like, EF-Tu-bound, accommodation and peptidyl-transfer states. The maps with the vacant and tRNA-bound E site were similarly resolved. In the E-tRNA bound states, non-cognate tRNA does not base-pair with the E-site codon (AAA), similarly to that in previous structures[64]. Unlike the well-resolved P-site and A-site tRNAs, the identities of the E-tRNA nucleotides could not be unambiguously ascribed to $tRNA^{fMet}$ or $tRNA^{Phe}$ owing to lower resolution, consistent with conformational and compositional heterogeneity. Both particle populations and visual inspection of the maps with the vacant E and tRNA-bound E site do not reveal obvious correlations with the occupancy or with structural features of the 30S A site or EF-Tu, suggested by the allosteric three-site model[65,66]. Although our observations are consistent with biochemical[67,68] and biophysical[69] findings of the absence of the allosteric interaction between the E and A sites, non-cognate E-tRNA in our study prevents us from directly addressing the allostery hypothesis.

Classification of the near-cognate dataset. The near-cognate dataset was processed in a similar fashion (Extended Data Fig. 2a) except that the EF-Tu-bound particles were processed independently and 3D masking was used to separate open and closed states of the 30S ribosomal subunit for states nc-IV and nc-V. First, EF-Tu-bound particles from classification 1 were extracted using merge_classes.exe including particles with greater than 50% occupancy and scores greater than 0 (11,091 particles). Multiple strategies were attempted to find particles with a closed 30S domain. First, the particles were separated into two or four classes using a 3D mask that included the shoulder domain of the 30S subunit. Although classes with an intermediate domain closure were apparent, no class with a fully closed 30S domain with residues 1492 and 1493 in the ON conformation emerged. Alternatively, a small focus mask (30 Å radius) around EF-Tu was used to separate particles into 4–8 classes on the basis of EF-Tu features. Classification was limited to 12 Å resolution and 50–100 rounds. Classification into 6 models yielded the most interpretable classes. These classes revealed EF-Tu conformations such as GTP-like conformation with an ordered or disordered switch I region, the extended post-hydrolysis conformation, and a pre-release conformation including a weak domain 2 matching those previously observed in the cognate data. In this classification too, none of the near-cognate EF-Tu maps had a closed 30S conformation. To quantify differences between EF-Tu states in the near-cognate and cognate datasets, the cognate 29-s data were processed identically to the near-cognate 30-s dataset using 6 models and the 30-Å focus mask. In addition to the classes described above for the near-cognate, a class with EF-Tu at the SRL and the 30S in the closed conformation was readily apparent in the cognate dataset. The percentage of 70S particles assigned to these classes is quantified in Fig. 3l and Extended Data Fig. 7b. Separation of near-cognate accommodation and peptidyl transfer states benefitted from a 3D mask around the shoulder domain of the 30S rather than focus masks as used in the cognate dataset. This type of classification revealed differences in the rotation of the 30S and 30S domain opening. To answer the question of whether domain opening occurs during accommodation with cognate tRNA (Fig. 3l), particles belonging to the cognate 29-s elbow accommodation states were also separated with the 3D mask around the shoulder into either 2 or 6 classes, but an open 30S was not observed.

Assessing optimal reconstruction parameters for low-population classes using a test with simulated stacks or using classes II-A and IV-A. *Test with simulated stacks.* Because our classifications yielded several classes comprising fewer than 10,000 particles (see below),

we tested which approach to particle parameter (orientation and shift) refinements yields most resolved maps. Specifically, we asked how the maps with original particle orientation parameters (that is, entire stack aligned together then no orientation refinement after classification) compare with those in which particle orientation parameters are refined after classification. Here we describe a simulation in which we also asked whether and how the number of particles affects the resolution of the maps. To this end, we tested three approaches, using Frealign v.9.11, cisTEM -1.0.0-beta[70] and Relion-3-beta[71] to process particle stacks with different numbers of particles. To ensure that the different particle stacks contain particles with similar structural features (that is, the same structure class) to allow map comparisons, they were generated from a single large high-resolution stack of 31,232 particles (class V-A; 3.2 Å average resolution) in triplicates, yielding stacks of approximately 500, 1,000, 2,000, 4,000, 8,000 and 16,000 particles (18 stacks in total). To this end, the occupancy column of the Frealign parameter file was replaced with random numbers from 0–100, and the stacks and parameter files of appropriate sizes were extracted by varying the occupancy threshold using merge_classes.exe.

For each substack, we next obtained reconstructions using: 1) FrealignX_calc_reconstruction (using the original particle orientation parameters determined before classification), 2) cisTEM's autorefine procedure with "Initial Res. Limit" set either to (a) 60 Å to match initial resolution in the Relion procedure or to (b) 50 Å, which resulted in improved maps for small stacks; or 3) Relion 3D autorefine procedure with default parameters. Procedure 1 is identical to our typical map calculations, described above, in that the original refinement (orientation and shift) parameters were used to create 1× binned reconstructions. Procedures 2a and 2b in cisTEM were used to determine and refine the orientation and shift parameters independently for each substack, using default cisTEM settings. The reference for particle alignment was EMD-1003 prepared in EMAN2 by changing pixel size. Procedure 3 in Relion was performed with default settings to determine the orientation and shift parameters and limit data resolution according to 'gold-standard' settings. The reference for particle alignment was filtered to 60 Å as per default settings in Relion. For all procedures, the final resolution was obtained from the masked reconstruction (FSC_part in Frealign/cisTEM or post-process step in Relion), without additional beam-tilt or other corrections.

This test revealed that the average map resolutions decrease with decreasing number of particles, consistent with published results[72]. Notably, post-classification particle parameter refinement (procedures 2 and 3) is detrimental for smaller stacks, resulting in poorly resolved maps, as described in the next paragraph. Furthermore, the resolutions estimated from triplicate stacks are highly variable for small stacks (ranging from 6 Å to 21 Å for 1,000 and 500 particles), further emphasizing suboptimal particle parameter refinement when the particle numbers are low. Instead, original orientation parameters (procedure 1) result in interpretable maps with well-resolved features even for 500 particles (around 4.84 ± 0.09 Å resolution).

By contrast, for the reconstructions calculated for the full large stack of 31,232 particles with the original and refined particle parameters, the map quality and resolutions were similar: 3.40 Å (procedure 1), 3.37 Å (procedure 2) and 3.76 Å (procedure 3). The performance of Relion may be suboptimal in our tests because we have not used the complete particle-picking and data processing pipeline in the program, to ensure that the same particles are used here in all three procedures. Nevertheless, the trends observed for Relion-processed data were similar to those for Frealign- and cisTEM-processed data. In general, our classification attempts in GPU-accelerated Relion with default parameters yielded high-quality initial reconstructions, similar to those in Frealign and cisTEM, but did not separated the classes as efficiently as Frealign. Frealign was more time-efficient than cisTEM or Relion, enabling us to test and compare numerous classification approaches, and thus representing an optimal classification strategy.

Maps with the original and refined particle parameters differed most for the stacks with fewer than 4,000 particles. At 4,000 particles, the resulting maps show similar resolutions for procedures 1 and 2a and 2b (3.87 ± 0.02 Å (1), 3.97 ± 0.05 Å (2a) and 4.06 ± 0.05 Å (2b), respectively) and a lower resolution for procedure 3 (5.01 ± 0.03 Å). Maps obtained for 2,000 particles had substantially more diverging resolution estimates from the triplicates in each approach, and particle-parameter refinement yielded less-resolved maps (4.14 ± 0.05 Å (1), 4.53 ± 0.11 Å (2a), 4.37 ± 0.06 (2b) and 6.7 ± 0.07 Å (3)). At 1,000 and 500 particles, the differences in resolution and map quality were even more pronounced (1,000 particles: 4.46 ± 0.06 Å (1), 14.12 ± 7.5 Å (2a), 5.21 ± 0.2 (2b) and 9.22 ± 0.2 Å (3); 500 particles: 4.84 ± 0.09 Å (1), 20.5 ± 1.3 Å (2a), 8.0 ± 4.1 (2b) and 12.3 ± 2.6 Å (3)). Visual inspection of the small-stack maps confirmed that the procedure using original refinement parameters (1) resulted in superior maps, which retained some higher-resolution features such as RNA nucleotide separation, unlike the procedures with orientation parameters refined for individual substacks (2a, 2b and 3).

Refinement of particle parameters for II-A and IV-A. In parallel with the simulation test, we tested the three reconstruction and refinement procedures described above on the classification-derived states with different numbers of particles: II-A (7,320 particles) and IV-A (1,471 particles). Similarly to the simulation results for the least-populated stacks, reconstructions for the sparse class IV-A are most well resolved with the default original particle parameters, whereas post-classification particle parameter refinement is detrimental to map quality. Specifically, our default reconstruction with subsequent beam-tilt corrections yielded a 4.0 Å (average resolution) reconstruction (map 1). Visual inspection confirmed that local features correspond to this average resolution, with some regions containing higher-resolution features, such as separated stacked nucleotides. Being part of the larger stack, the particles in this class have partial occupancies (calculated by frealign_run_refine in the original refinement procedure), and frealign_calc_stats reports that they correspond to 1,471 particles. To test particle parameter refinement in cisTEM (procedure 2) and Relion (procedure 3), we extracted particles belonging to state IV-A using merge_classes.exe including particles with greater than 50% occupancy and scores greater than 0, yielding a 1,790 particle stack with occupancies reset to 100%. This stack was imported with contrast transfer function (CTF) parameters into cisTEM and refined against EMD-1003 using default auto-refine parameters, followed by beam-tilt correction, yielding a map at 4.63 Å resolution (map 2). Similarly we exported the stack and par file to Relion and performed 3D-autorefine against EMD-1003 as a reference using default parameters, followed by beam-tilt refinement, 3D-autorefine and post-processing (all steps in Relion), yielding a 6.61 Å reconstruction (map 3). Both cisTEM and Relion maps contained similar lower-resolution features, including EA-1 tRNA, but lacked high-resolution detail, indicating suboptimal particle parameter refinement, probably owing to the small particle number. Indeed, for the modestly populated class II-A of more than 7,000 particles, the map resolutions and structural details were improved to 3.6 Å (procedure 1), 3.8 Å (procedure 2) and 4.9 Å (procedure 3). Nevertheless, visual inspection confirmed that both the highly resolved regions (for example, peptidyl transferase centre) and the less-resolved features (for example, secondary structure of peripheral proteins) were superior in map 1 obtained with the original particle parameters.

Finalizing maps. After the final classifications were completed, we were able to improve each map by 0.1–0.4 Å by applying a beam tilt correction using cisTEM[70]. The beam tilt parameters were calculated once for each dataset using all particles and then were applied to the classified maps. In the case of EF-Tu, where three datasets were joined, the beam tilt parameters were calculated using the 79,838 EF-Tu bound particle stack then applied to each of the 10 classes described in the text.

FSC curves were calculated by Frealign (FSC_part) for even and odd particle half-sets (Extended Data Figs. 1c–f, 2b). The maps used for

structure docking and refinement were softened or sharpened by using bfactor.exe, part of the FREALIGN v9.11 distribution.

To assess the local resolution of the cryo-EM maps and filter them for structure refinements, we used blocres and blocfilt from the Bsoft package[73], after testing several local-resolution filtering approaches. In brief, a mask was created for each map by low-pass filtering the map to 30 Å in Bsoft, then binarizing, expanding by 3 pixels and applying a 3-pixel Gaussian edge in EMAN2. Blocres was run with a box size of 26 pixels for maps with average resolutions near 4 Å, or a box size of 20 pixels for maps I-A, V-A, V-B, VI-A and VI-B with resolutions closer to 3 Å. In each case, the resolution criterion was FSC with a cutoff of 0.143. The output of Blocres was used to filter maps according to local resolution using blocfilt. Visual inspections and structure refinements against (1) original Frealign maps, (2) blocfilt maps and (3) blocfilt maps followed by filtering with different B-factors at different resolutions revealed that optimal balance between high-resolution and lower-resolution regions is achieved for blocfilt maps filtered with a constant B-factor of −50 Å^2 to the average resolution as determined by FSC_part. These maps were used for final structure refinements (Supplementary Tables 1–3). Local regions described in the manuscript were nevertheless inspected using a series of maps (for each class) obtained with different filtering approaches to minimize bias in interpretation.

Model building and refinement

The 3.2-Å cryo-EM structure of 70S•tRNA•EF-Tu•GDPCP (PDB: 5UYM[5]) was used as a starting model for structure refinements. A*/T for structures II-A to II-D was adopted from PDB: 5UYL[5]. The starting model for domain 1 of EF-Tu bound with GDP was taken from PDB: 1DG1[74]. The starting models for the EA, A/A, and A/P tRNA^{Phe} were adapted from PDB: 1VY5[75]. fMet and Phe and fMet-Phe dipeptide were adapted from PDB: 1VY4 and PDB: 1VY5[75]. E-site tRNA was modelled as tRNA^{fMet} (ref. [5]). E/P tRNA^{fMet} was modelled using PDB: 4V80[76] whereas H69 of 23S rRNA in the hybrid states was modelled using PDB: 4V9D[18]. All structures were domain-fitted using Chimera[77] and refined using real-space simulated-annealing refinement using RSRef[78,79] against corresponding maps. Local structural elements that differed between structures, such as the decoding centre or mRNA codon, were manually fitted and modelled into cryo-EM maps in PyMOL[80] and Coot[81]. Refinement parameters, such as the relative weighting of stereochemical restraints and experimental energy term, were optimized to produce the optimal structure stereochemistry, real-space correlation coefficient and *R*-factor, which report on the fit of the model to the map[82]. Lower-resolution (approximately 4 Å) structures were refined conservatively and visual inspection confirmed good fits. Secondary-structure restraints, comprising hydrogen-bonding restraints for ribosomal proteins and base-pairing restraints for RNA molecules were used as described[83] and allowed for a conservative and stereochemically restrained refinement into lower-resolution maps. The structures were next refined using phenix.real_space_refine[84] followed by a round of refinement in RSRef applying harmonic restraints to preserve protein backbone geometry[78,79]. Phenix was used to refine B-factors of the models against their respective maps[84]. The resulting structural models have good stereochemical parameters, characterized by low deviation from ideal bond lengths and angles and agree closely with the corresponding maps as indicated by high correlation coefficients and low real-space R factors (Supplementary Tables 1, 2, 3). Visual inspection of key functional regions was performed for each structure to ensure reasonable fits.

Structure superpositions and distance calculations were performed in PyMOL. To calculate an angle of the 30S subunit rotation for accommodation and peptidyl-transfer states with respect to structure III-B, 23S rRNAs were aligned with 23S rRNA from structure III-B using PyMOL, and the angle between 16S body regions (residues 2–920 and 1398–1540) was measured in Chimera. Figures were prepared in PyMOL and Chimera.

Data reporting

No statistical methods were used to predetermine sample size. The experiments were not randomized and the investigators were not blinded to allocation during experiments and outcome assessment.

Reporting summary

Further information on research design is available in the Nature Research Reporting Summary linked to this paper.

Data availability

The models generated and analysed during the current study are available from the RCSB PDB: 6WD0 (structure I-A), 6WD1 (structure I-B), 6WD2 (structure II-A), 6WD3 (structure II-B1), 6WD4 (structure II-B2), 6WD5 (structure II-C1), 6WD6 (structure II-C2), 6WD7 (structure II-D), 6WD8 (structure III-A), 6WD9 (structure III-B), 6WDA (structure III-C), 6WDB (structure IV-A), 6WDC (structure IV-B), 6WDD (structure V-A), 6WDE (structure V-B), 6WDF (structure VI-A), 6WDG (structure VI-B), 6WDH (structure IV-B1-nc), 6WDI (structure IV-B2-nc), 6WDJ (structure V-A1-nc), 6WDK (structure V-A2-nc), 6WDL (structure V-B1-nc) and 6WDM (structure V-B2-nc). The cryo-EM maps used to generate models are available from the EMDB: EMD-21619 (structure I-A), EMD-21620 (structure I-B), EMD-21621 (structure II-A), EMD-21622 (structure II-B1), EMD-21623 (structure II-B2), EMD-21624 (structure II-C1), EMD-21625 (structure II-C2), EMD-21626 (structure II-D), EMD-21627 (structure III-A), EMD-21628 (structure III-B), EMD-21629 (structure III-C), EMD-21630 (structure IV-A), EMD-21631 (structure IV-B), EMD-21632 (structure V-A), EMD-21633 (structure V-B), EMD-21634 (structure VI-A), EMD-21635 (structure VI-B), EMD-21636 (structure IV-B1-nc), EMD-21637 (structure IV-B2-nc), EMD-21638 (structure V-A1-nc), EMD-21639 (structure V-A2-nc), EMD-21640 (structure V-B1-nc) and EMD-21641 (structure V-B2-nc).

52. Svidritskiy, E. & Korostelev, A. A. Conformational control of translation termination on the 70S ribosome. *Structure* **26**, 821–828.e3 (2018).
53. Lancaster, L. & Noller, H. F. Involvement of 16S rRNA nucleotides G1338 and A1339 in discrimination of initiator tRNA. *Mol. Cell* **20**, 623–632 (2005).
54. Walker, S. E. & Fredrick, K. Preparation and evaluation of acylated tRNAs. *Methods* **44**, 81–86 (2008).
55. Mastronarde, D. N. Automated electron microscope tomography using robust prediction of specimen movements. *J. Struct. Biol.* **152**, 36–51 (2005).
56. Kremer, J. R., Mastronarde, D. N. & McIntosh, J. R. Computer visualization of three-dimensional image data using IMOD. *J. Struct. Biol.* **116**, 71–76 (1996).
57. Rohou, A. & Grigorieff, N. CTFFIND4: Fast and accurate defocus estimation from electron micrographs. *J. Struct. Biol.* **192**, 216–221 (2015).
58. Chen, J. Z. & Grigorieff, N. SIGNATURE: a single-particle selection system for molecular electron microscopy. *J. Struct. Biol.* **157**, 168–173 (2007).
59. Gabashvili, I. S. et al. Solution structure of the *E. coli* 70S ribosome at 11.5 A resolution. *Cell* **100**, 537–549 (2000).
60. Tang, G. et al. EMAN2: an extensible image processing suite for electron microscopy. *J. Struct. Biol.* **157**, 38–46 (2007).
61. Lyumkis, D., Brilot, A. F., Theobald, D. L. & Grigorieff, N. Likelihood-based classification of cryo-EM images using FREALIGN. *J. Struct. Biol.* **183**, 377–388 (2013).
62. Wieden, H. J., Wintermeyer, W. & Rodnina, M. V. A common structural motif in elongation factor Ts and ribosomal protein L7/12 may be involved in the interaction with elongation factor Tu. *J. Mol. Evol.* **52**, 129–136 (2001).
63. Cornish, P. V., Ermolenko, D. N., Noller, H. F. & Ha, T. Spontaneous intersubunit rotation in single ribosomes. *Mol. Cell* **30**, 578–588 (2008).
64. Jenner, L. B., Demeshkina, N., Yusupova, G. & Yusupov, M. Structural aspects of messenger RNA reading frame maintenance by the ribosome. *Nat. Struct. Mol. Biol.* **17**, 555–560 (2010).
65. Nierhaus, K. H. The allosteric three-site model for the ribosomal elongation cycle: features and future. *Biochemistry* **29**, 4997–5008 (1990).
66. Dinos, G., Kalpaxis, D. L., Wilson, D. N. & Nierhaus, K. H. Deacylated tRNA is released from the E site upon A site occupation but before GTP is hydrolyzed by EF-Tu. *Nucleic Acids Res.* **33**, 5291–5296 (2005).
67. Semenkov, Y. P., Rodnina, M. V. & Wintermeyer, W. The "allosteric three-site model" of elongation cannot be confirmed in a well-defined ribosome system from *Escherichia coli*. *Proc. Natl Acad. Sci. USA* **93**, 12183–12188 (1996).
68. Petropoulos, A. D. & Green, R. Further in vitro exploration fails to support the allosteric three-site model. *J. Biol. Chem.* **287**, 11642–11648 (2012).
69. Uemura, S. et al. Real-time tRNA transit on single translating ribosomes at codon resolution. *Nature* **464**, 1012–1017 (2010).

70. Grant, T., Rohou, A. & Grigorieff, N. cisTEM, user-friendly software for single-particle image processing. *eLife* **7**, e35383 (2018).
71. Zivanov, J. et al. New tools for automated high-resolution cryo-EM structure determination in RELION-3. *eLife* **7**, e42166 (2018).
72. Passos, D. O. & Lyumkis, D. Single-particle cryoEM analysis at near-atomic resolution from several thousand asymmetric subunits. *J. Struct. Biol.* **192**, 235–244 (2015).
73. Cardone, G., Heymann, J. B. & Steven, A. C. One number does not fit all: mapping local variations in resolution in cryo-EM reconstructions. *J. Struct. Biol.* **184**, 226–236 (2013).
74. Abel, K., Yoder, M. D., Hilgenfeld, R. & Jurnak, F. An alpha to beta conformational switch in EF-Tu. *Structure* **4**, 1153–1159 (1996).
75. Polikanov, Y. S., Steitz, T. A. & Innis, C. A. A proton wire to couple aminoacyl-tRNA accommodation and peptide-bond formation on the ribosome. *Nat. Struct. Mol. Biol.* **21**, 787–793 (2014).
76. Jin, H., Kelley, A. C. & Ramakrishnan, V. Crystal structure of the hybrid state of ribosome in complex with the guanosine triphosphatase release factor 3. *Proc. Natl Acad. Sci. USA* **108**, 15798–15803 (2011).
77. Pettersen, E. F. et al. UCSF Chimera—a visualization system for exploratory research and analysis. *J. Comput. Chem.* **25**, 1605–1612 (2004).
78. Korostelev, A., Bertram, R. & Chapman, M. S. Simulated-annealing real-space refinement as a tool in model building. *Acta Crystallogr. D* **58**, 761–767 (2002).
79. Chapman, M. S. Restrained real-space macromolecular atomic refinement using a new resolution-dependent electron-density function. *Acta Crystallogr. A* **51**, 69–80 (1995).
80. DeLano, W. L. *The PyMOL Molecular Graphics System*. (DeLano Scientific, 2002).
81. Emsley, P. & Cowtan, K. Coot: model-building tools for molecular graphics. *Acta Crystallogr. D* **60**, 2126–2132 (2004).
82. Zhou, G., Wang, J., Blanc, E. & Chapman, M. S. Determination of the relative precision of atoms in a macromolecular structure. *Acta Crystallogr. D* **54**, 391–399 (1998).
83. Laurberg, M. et al. Structural basis for translation termination on the 70S ribosome. *Nature* **454**, 852–857 (2008).
84. Adams, P. D. et al. The Phenix software for automated determination of macromolecular structures. *Methods* **55**, 94–106 (2011).
85. Gao, Y. G. et al. The structure of the ribosome with elongation factor G trapped in the posttranslocational state. *Science* **326**, 694–699 (2009).
86. Diaconu, M. et al. Structural basis for the function of the ribosomal L7/12 stalk in factor binding and GTPase activation. *Cell* **121**, 991–1004 (2005).
87. Leijonmarck, M. & Liljas, A. Structure of the C-terminal domain of the ribosomal protein L7/L12 from *Escherichia coli* at 1.7 A. *J. Mol. Biol.* **195**, 555–579 (1987).

Acknowledgements We thank M. Rigney for help with grid preparation and screening at the cryo-EM facility at Brandeis University; C. Xu and K. Song for data collection at the cryo-EM facility at UMass Medical School; D. Conte Jr., D. Ermolenko, A. Korennykh and members of the Korostelev laboratory for comments on the manuscript; and D. Grunwald and D. Susorov for help with the video. This study was supported by NIH grants R01 GM106105, R01 GM107465 and R35 GM127094 (to A.A.K.). A.B.L. performed part of this work as a Howard Hughes Medical Institute Fellow of the Helen Hay Whitney Foundation.

Author contributions A.B.L. and A.A.K. developed the concept of the work. A.B.L., G.D. and A.A.K. designed the methodology. A.B.L. and A.A.K. validated the methodology. A.B.L. and G.D. carried out the experiments. A.A.K. provided resources. A.B.L. and A.A.K. wrote the original draft of the manuscript; A.B.L., G.D. and A.A.K. reviewed and edited the manuscript. A.B.L. generated graphics and figures for the manuscript. A.A.K. acquired funding and supervised the project.

Competing interests The authors declare no competing interests.

Additional information

Supplementary information is available for this paper at https://doi.org/10.1038/s41586-020-2447-x.

Correspondence and requests for materials should be addressed to A.A.K.

Peer review information *Nature* thanks Yves Mechulam and the other, anonymous, reviewer(s) for their contribution to the peer review of this work.

Reprints and permissions information is available at http://www.nature.com/reprints.

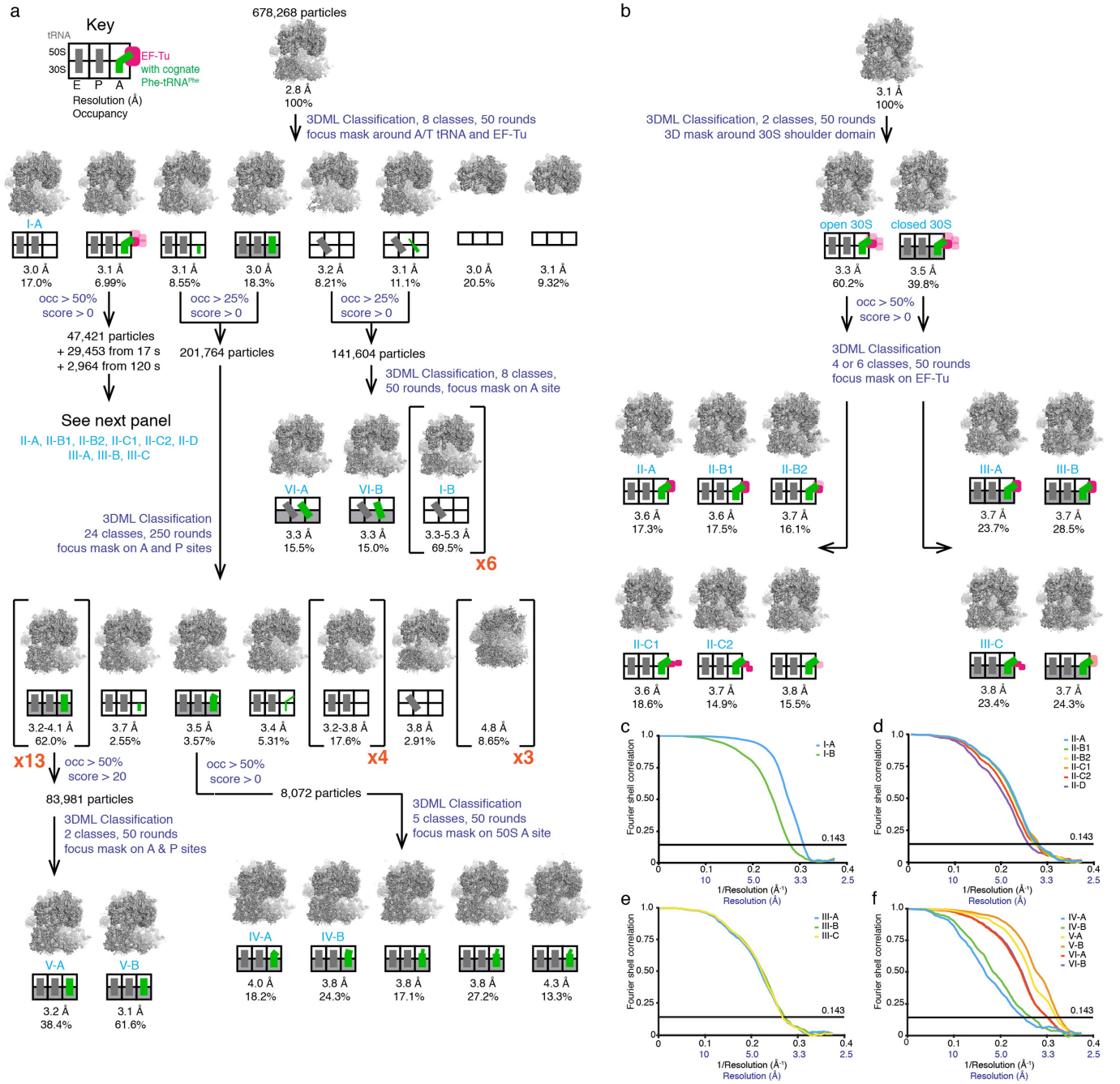

Extended Data Fig. 1 | Classification procedure and FSC curves for maps of cognate ternary complex decoding. a, Scheme of the maximum-likelihood classification strategy to obtain the final maps and state occupancies for the cognate 29-s dataset. Transparency for EF-Tu and line-thickness for tRNA depict full/partial occupancy or strong/weak features. Gray shading in 30S subunit indicates the closed 30S subunit conformation. Brackets with red multiplication signs (*e.g. x3*), indicate the number of states that recur, and in such cases the lowest and highest resolution is listed along with a summed occupancy for all states. **b**, EF-Tu-bound particles from 17 s, 29 s and 120 s were processed together to obtain final maps for states II-A to III-C. **c**–**f**, Fourier shell correlations (FSC) between even- and odd-particle half maps show that average resolutions range from 3.0 to 4.0 Å for modelled maps. **c**, Substrate ribosome states. **d**, EF-Tu-bound ribosome states with an open 30S subunit. **e**, EF-Tu-bound ribosome states with a closed 30S subunit. **f**, Accommodation and product ribosome states.

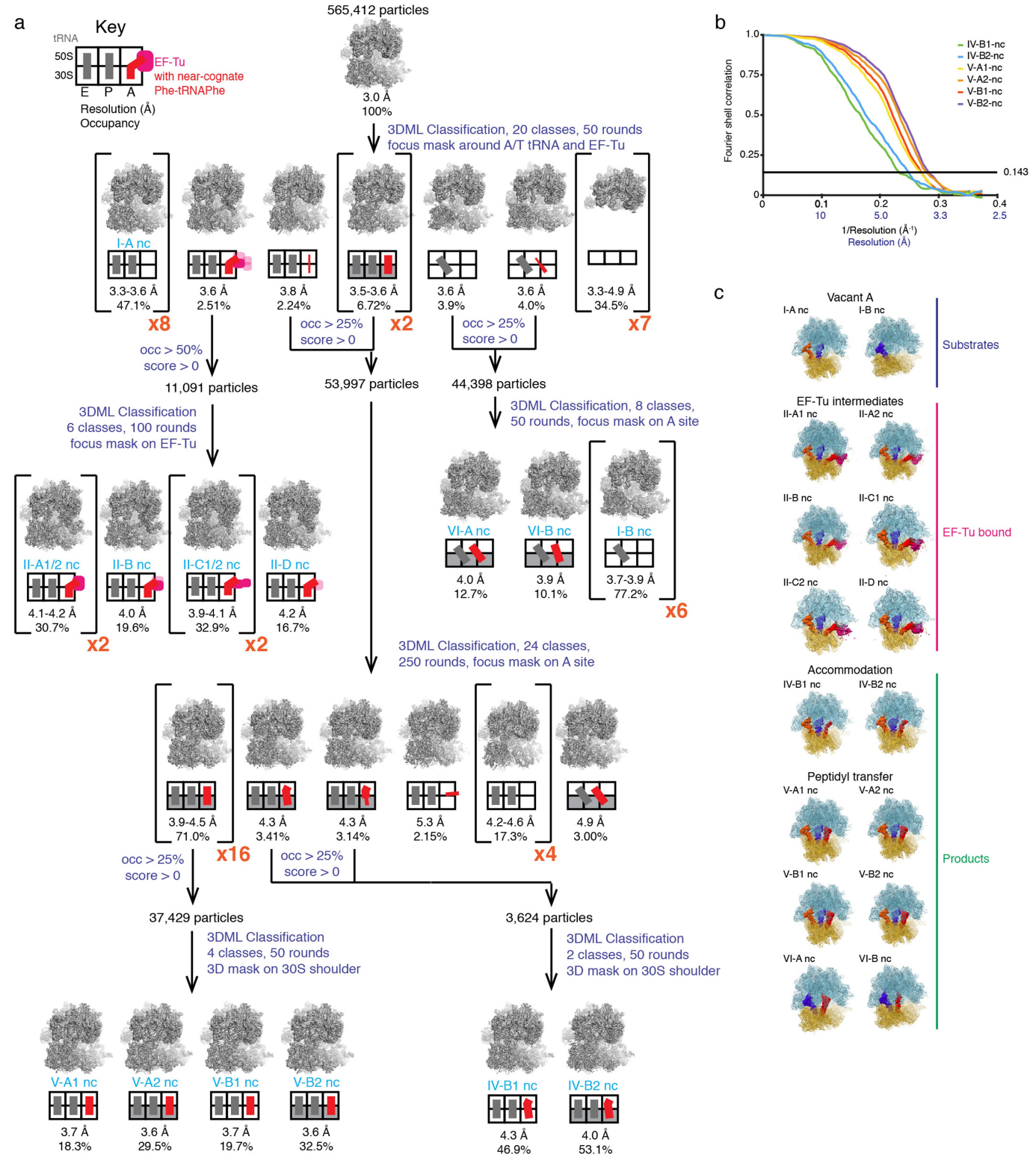

Extended Data Fig. 2 | Classification procedure and FSC curves for maps of near-cognate ternary complex decoding. a, Scheme depicts maximum-likelihood classification strategy to obtain the final maps and state occupancies for the near-cognate 30-s dataset. **b**, Fourier shell correlation (FSC) between even- and odd-particle half maps for near-cognate ribosome states that were modelled. **c**, Cryo-EM maps for 16 states of the elongation reaction with near-cognate tRNA, and their assignment as substrates, EF-Tu-bound intermediates, or products of the reaction. The maps are coloured to show the 50S ribosomal subunit (light blue), 30S ribosomal subunit (yellow), E-tRNA (orange), P-tRNA (dark blue), near-cognate A-tRNA (red), and EF-Tu (magenta).

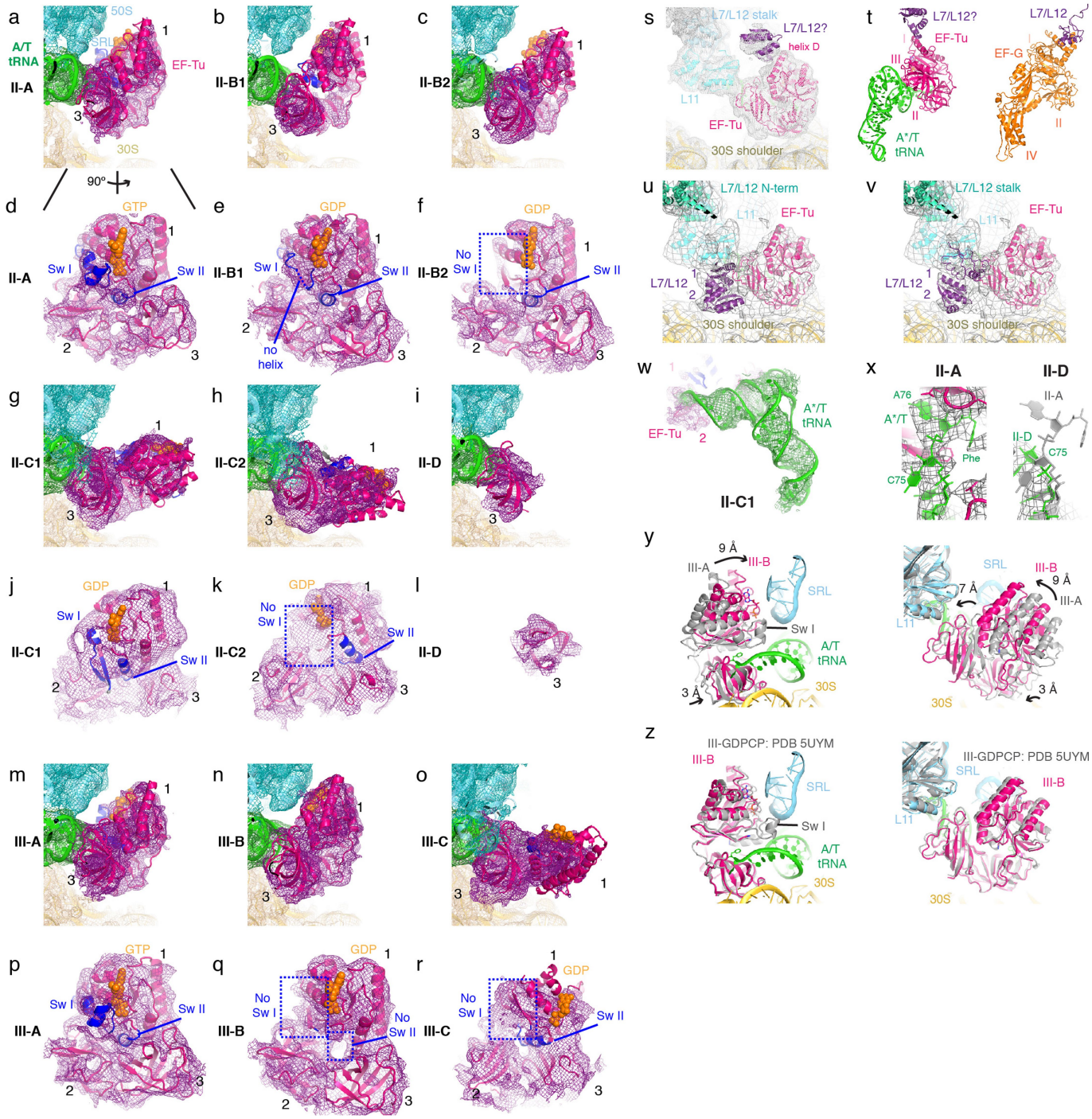

Extended Data Fig. 3 | See next page for caption.

Extended Data Fig. 3 | Cryo-EM density and interactions of EF-Tu. a–**r**, Density for EF-Tu in 30S-open (II) and 30S-closed (III) conformations is shown relative to the sarcin-ricin loop (SRL) (**a**–**c**, **g**–**i** and **m**–**o**) or at the tRNA interacting face (**d**–**f**, **j**–**l** and **p**–**r**; tRNA is omitted for clarity). Maps were filtered according to local resolution, using blocfilt (Methods). Numbers 1–3 indicate domains of EF-Tu. EF-Tu is shown in magenta with switch I region (Sw I) and switch II region (Sw II) shown in blue, tRNA is shown in green, 30S subunit is shown in gold, 50S subunit is shown in cyan. **a**, Map II-A (shown at 3σ). **b**, Map II-B1 (3.25σ). **c**, Map II-B2 (2.5σ). **d**, Map II-A has strong density for both switch I and switch II regions (2σ). **e**, Map II-B1 has weaker density for switch I (2σ). **f**, In map II-B2, density for switch I is missing even at lower contour levels (shown at 1.5σ). **g**, Map II-C1 (1σ). **h**, Map II-C2 (1σ). **i**, Map II-D has only domain 3 density at low contour levels (0.5σ). **j**, Map II-C1 has only weak density for switch I and switch II (0.25σ). **k**, Map II-C2 is missing ordered density for most of switch I (0.5σ). **l**, Map II-D has weak density only for domain 3 (0.5σ). **m**, Map III-A shows EF-Tu away from the SRL when the 30S closure is intermediate (2σ). **n**, Map III-B shows EF-Tu next to the SRL, when 30S subunit is in the closed conformation (2σ). **o**, Map III-C shows GTPase domain away from the SRL and rotated by approximately 90° relative to domain 2 (1.5σ). **p**, Map III-A has density for both switch I and switch II (1.5σ). **q**, In map III-B, density for both switch I and switch II is missing (1.5σ). **r**, Map III-C has weak density for switch I (1.25σ). **s**, Classification with a larger mask around EF-Tu reveals a map with weak density at helix D of domain 1, which corresponds to the binding site for the C terminus of L7/L12. Map was low-pass filtered to 6 Å and is shown at 1σ. **t**, The putative interaction of L7/L12 with domain 1 of EF-Tu (left) differs from that of L7/L12 with domain 1 of EF-G (right). Rigid-body fitted structure of EF-Tu and L7/L12 as in **a** was aligned to EF-G from PDB: 4V5F[85] via GTPase domains. **u**, **v**, An independent classification strategy yielded a map (shown with 4× binning and at 0.75σ) with density sufficient to fit a dimer of the L7/L12 C-terminal domain. The density bridges domain 3 of EF-Tu with L11. Model for L7/L12 N terminus (green cyan) from PDB:1ZAX[86] is shown on both panels. **u**, Tentative fit utilizes the L7/L12 dimer interface observed in the X-ray crystallographic structure (PDB: 1CTF[87]). **v**, Alternatively, two monomers may be docked independently (bottom based on PDB: 1CTF) and top based on PDB: 4V5F). **w**, Cryo-EM map II-C1 shows ordered density for A*/T tRNA when EF-Tu domain 1 undocks from the tRNA and SRL, while domain 2 (magenta) remains bound. Map is shown at 3σ for A*/T tRNA and 2σ for EF-Tu. **x**, Comparison between II-A and II-D shows that density is missing for A76 and Phe of Phe-tRNA^{Phe} upon release of EF-Tu domain 2 in II-D. Right, map II-A, filtered via blocfilt and B-factor sharpened (−75 Å^2), with ordered EF-Tu shows strong density for A76 and Phe (2.75σ). Left, map II-D was filtered via blocfilt and B-factor sharpened (−50 Å^2) and is shown at 0.75σ to accentuate weak density. A*/T tRNA from II-A is shown in grey for reference after structural superposition of structures via 23S rRNA. **y**, Comparison of EF-Tu in structure III-A (resembling a pre-GTP-hydrolysis state, grey, only EF-Tu is shown) and III-B (post-GTP hydrolysis, coloured as in Fig. 1) reveals roles of the 30S shoulder in bringing EF-Tu towards the SRL and of L11 in optimally positioning EF-Tu for GTP hydrolysis. Alignment of structures was achieved by superposition of 23S rRNA. **z**, Superposition shows similarity of structure III-B (coloured) with 70S•Phe-tRNA^{Phe}•EF-Tu stalled with GDPCP in previous work (PDB: 5UYM[5]).

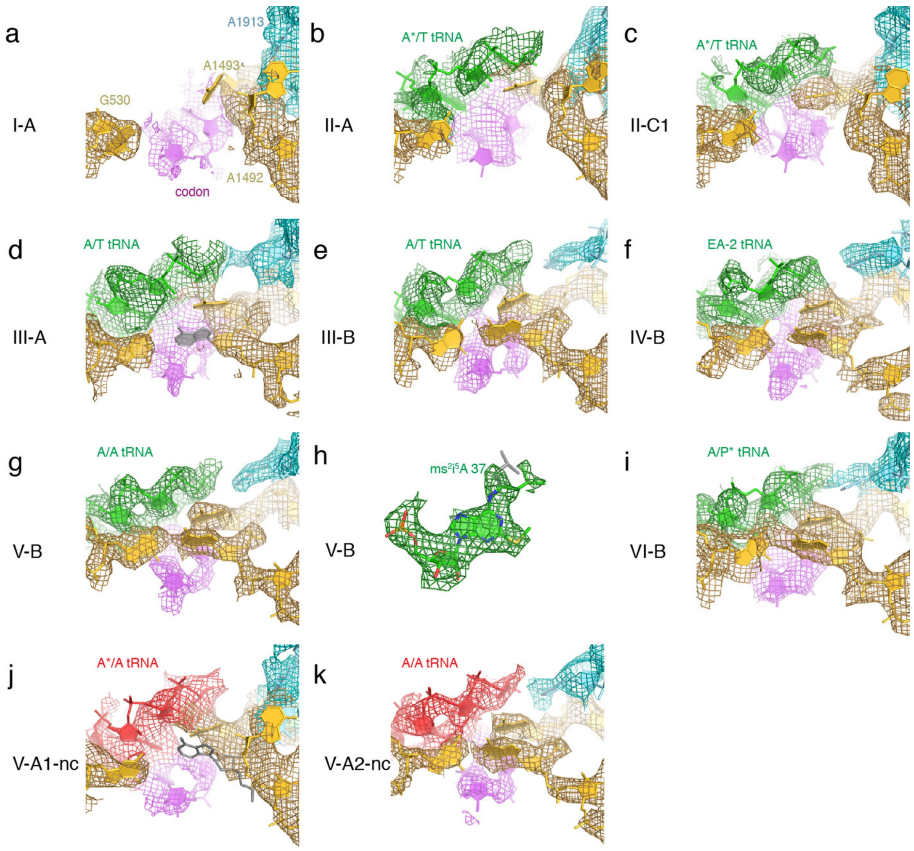

Extended Data Fig. 4 | Cryo-EM density of the decoding centre of the open and closed 30S conformations. 16S rRNA is shown in yellow, 23S rRNA is shown in cyan, codon is shown in magenta, cognate tRNA is shown in green and near-cognate tRNA is shown in red. All maps have been local-resolution-filtered using blocfilt and B-factor-sharpened (−75 Å^2). **a**, Structure I-A with the decoding centre in an open conformation; 16S residues of helix 44 including residues 1492–1493 are shown at 2.5σ, G530 of the 16S is shown at 4σ, 23S rRNA residue A1913 at 2.5σ, and the weaker codon density is shown at 1.0σ. **b**, Structure II-A with the decoding centre in an open conformation in the presence of A*/T tRNA; the codon and A*/T tRNA are shown at 2.5σ, h44 is shown at 2.5σ, G530 is shown at 4.5σ, A1913 is shown at 3σ. **c**, Structure II-C1 with the decoding centre in an open conformation in the presence of A*/T tRNA and with EF-Tu in an extended, post-GTP hydrolysis conformation; the codon and A*/T tRNA are shown at 3.75σ, h44 is shown at 2.5σ, G530 is shown at 3σ, A1913 is shown at 2.5σ. **d**, Structure III-A with the decoding centre in an intermediate conformation in the presence of A*/T tRNA; the codon and A*/T tRNA are shown at 3.5σ, h44 is shown at 3.5σ, G530 is shown at 5σ and A1913 at 2.5σ. **e**, Structure III-B with a closed conformation of the decoding centre in the presence of A/T tRNA; the codon and A/T tRNA are shown at 4.5σ, h44 is shown at 4.5σ, G530 is shown at 5σ and A1913 is shown at 5σ. **f**, Structure IV-B with the decoding centre in a closed conformation during accommodation; the codon, EA-1 tRNA, A1913 and 16S h44 are shown at 5σ, and G530 is shown at 6σ. **g**, Structure V-B with the decoding centre in a closed conformation in the presence of the accommodated A/A tRNA; the codon and A/A tRNA, 23S rRNA and G530 are shown at 5σ, and h44 at 4.5σ. **h**, Density for the modified nucleotide at position 37, 2-methylthio-N^6-(2-isopentenyl)-adenosine, of the anticodon in V-B (cryo-EM map was filtered with blocfilt and B-factor-sharpened (−100 Å^2) and is shown at 4σ). **i**, Structure VI-B with the decoding centre in a closed conformation in the presence of A/P* tRNA; the codon, A/T tRNA, h44 and G530 are shown at 3.5σ, and A1913 at 3σ. **j**, Near-cognate structure V-A1-nc with the decoding centre in an open conformation in the presence of A*/A tRNA with the accommodated CCA end; the codon and A*/A tRNA are shown at 3.75σ, h44 and A1913 are shown at 3.5σ and G530 is shown at 5σ. **k**, Near-cognate structure V-A2-nc with the decoding centre in a closed conformation in the presence of A/A tRNA; the codon and A/A tRNA are shown at 6σ, h44 is shown at 5σ, G530 at 7σ and A1913 at 3σ.

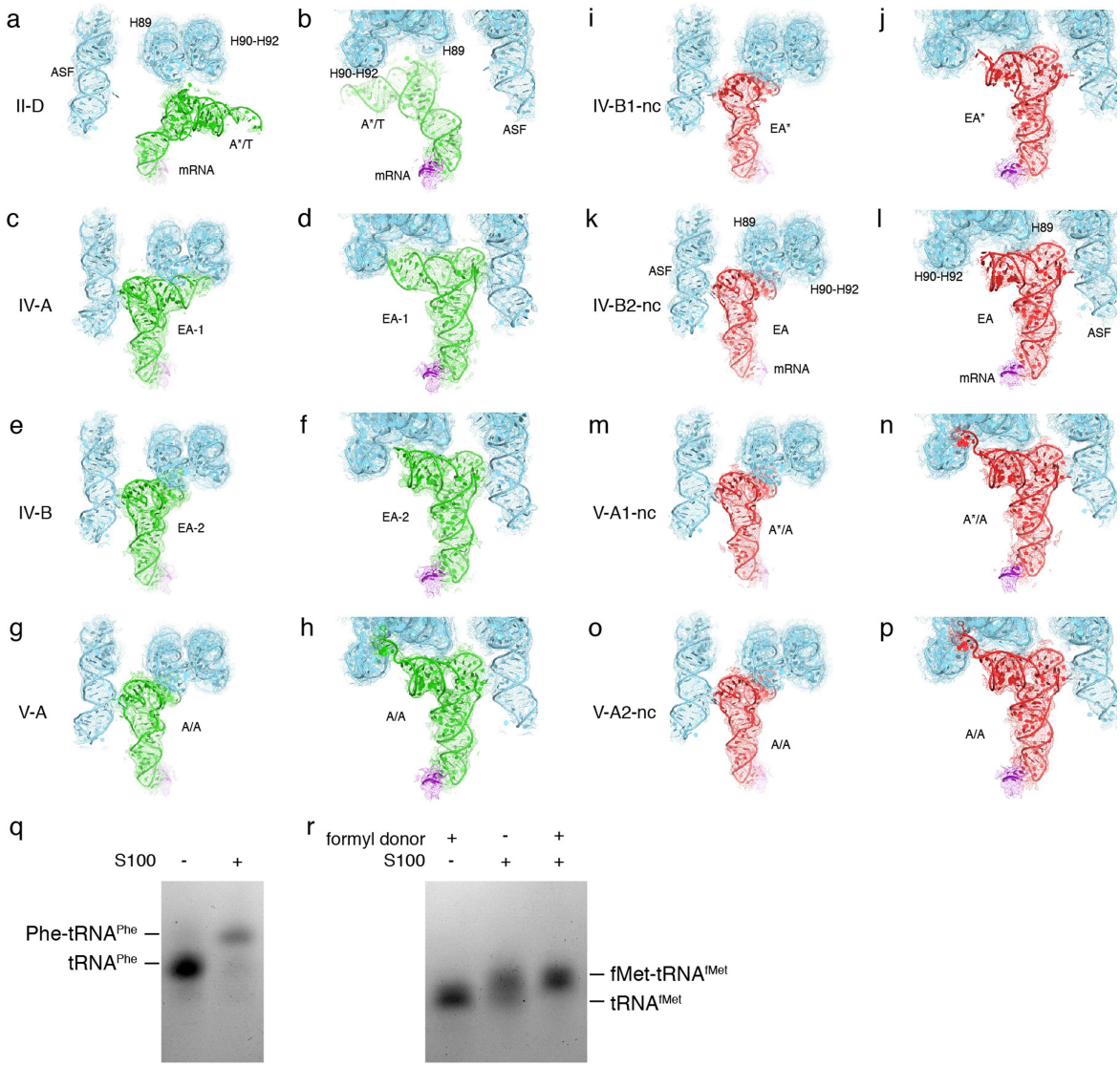

Extended Data Fig. 5 | Cryo-EM density for tRNAs during cognate and near-cognate tRNA decoding. Cognate tRNA is shown in green, near-cognate tRNA is shown in red, 23S rRNA including ASF (residues 860:915), H89 (residues 2450–2500), and H90–H92 (residues 2513:2571) are shown in cyan, and the mRNA codon is shown in magenta. Cryo-EM maps were local-resolution-filtered using blocfilt. **a**, **b**, Structure II-D and cryo-EM map shown at 2σ. **c**, **d**, Structure IV-A and cryo-EM map shown at 3σ. **e**, **f**, Structure IV-B and cryo-EM map shown at 3σ. **g**, **h** Structure V-A and cryo-EM map shown at 3σ. **i**, **j**, Structure IV-B1-nc and cryo-EM map shown at 2σ. **k**, **l**, Structure IV-B2-nc and cryo-EM map shown at 2σ. **m**, **n**, Structure V-A1-nc and cryo-EM map shown at 3σ. **o**, **p**, Structure V-A2-nc and cryo-EM map shown at 3σ. **q**, Charging of tRNA^{Phe} with phenylalanine, as assessed by 6.5% acid-PAGE and methylene-blue staining (see uncropped gel image in Supplementary Information). **r**, Charging of tRNA^{fMet} by formyl-methionine (as in **q**).

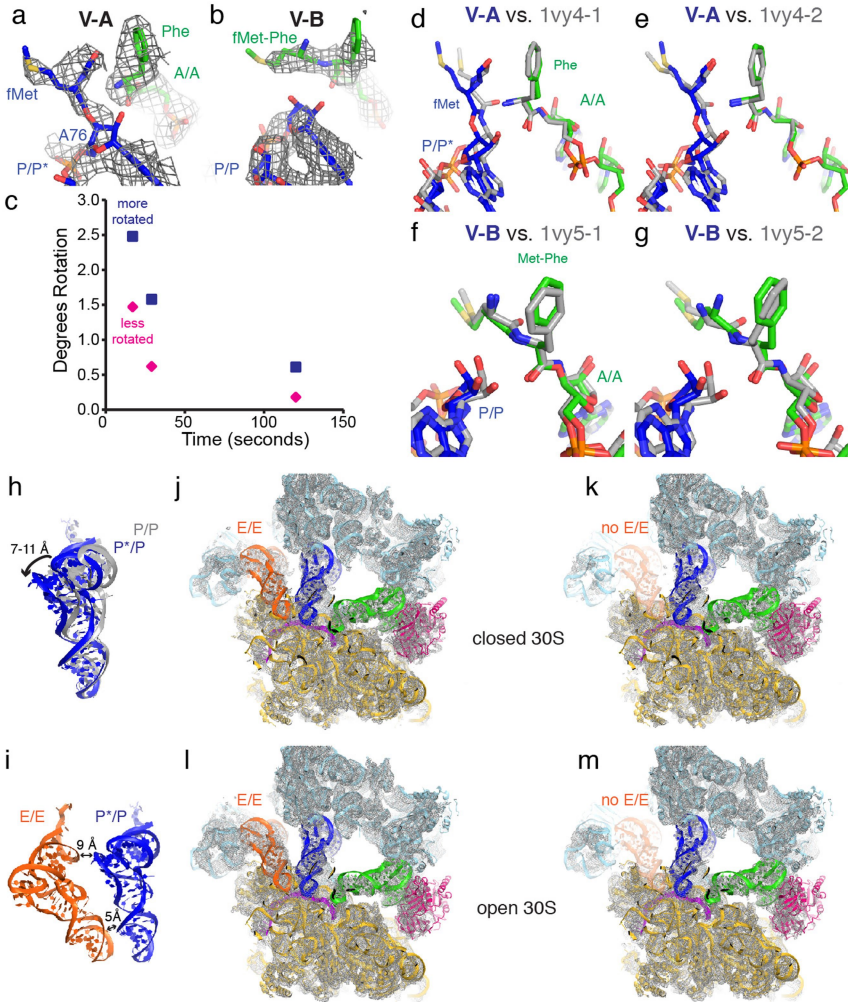

Extended Data Fig. 6 | 30S rotation in accommodation states and tRNA conformations in peptidyl-transfer states. a, In state V-A, with a partially rotated 30S subunit, cryo-EM density is consistent with substrate aminoacyl-tRNAs. Cryo-EM map was filtered with blocfilt and B-factor-sharpened (−50 Å^2) and is shown at 2.5σ. **b**, In state V-B, which is less rotated, cryo-EM density is consistent with product dipeptidyl-tRNA. Cryo-EM map was filtered with blocfilt and B-factor-sharpened (−50 Å^2) and is shown at 3.5σ. **c**, Change of the 70S conformation in accommodation intermediates over time. The 30S subunit rotation angle decreases with time in ribosome states with A/A-like tRNA, consistent with accommodation completion in a non-rotated state. Rigid-body docking of 50S subunit, 30S head, 30S shoulder, and 30S body was performed into the cryo-EM maps obtained for the 17- and 120-s time points. Superposition with the 70S•tRNA•EF-Tu•GDPCP structure (PDB: 5UYM[5],) was achieved by structural alignment of 23S rRNA. Rotation of the 30S body rRNA versus that of non-rotated (PDB: 5UYM) was determined in Chimera. **d**–**g**, Superpositions of the aminoacyl moieties in V-A and V-B with crystallographic structures of the *T. th.* 70S ribosome captured with substrate analogues (PDB: 1VY4) and product analogue (PDB: 1VY5)[75]. **d**, **e**, Substrate Phe-tRNA^{Phe} in A site (green) and fMet-tRNA^{fMet} (blue) in V-A are shown compared to two 70S structures in the asymmetric unit of PDB: 1VY4 (grey). Superposition was achieved by structural alignment of 23S rRNA. **f**, **g**, Product dipeptidyl fMet-Phe-tRNA^{Phe} in the A site (green) and deacylated P-tRNA^{fMet} (blue) in V-B are shown compared to two 70S structures in the asymmetric unit of PDB: 1VY5 (grey). In V-B, formyl group was not resolved. **h**, P*/P tRNA elbow (blue) in a partially rotated 30S conformation (V-A) is displaced by 7-11 Å towards the E site, relative to its position in the classical-state P/P tRNA (grey; V-B). Superposition of Structures V-A and V-B was achieved by structural alignment of 23S rRNA. **i**, P*/P tRNA (blue) is shown relative to the E-site tRNA (orange) in structure V-A. **j**, **k**, Particle classification yields E-site tRNA-bound (**j**) and vacant (**k**) particles with similar conformations of 30S-domain-closed complexes. Cryo-EM maps with or without E-tRNA (see Methods) were low-pass filtered to 4 Å and B-factor-softened (50 Å^2) and are shown at 3.2σ. **l**, **m**, Particle classification yields E-site tRNA-bound (**l**) and vacant (**m**) particles with similar conformations of 30S-domain-open complexes. Cryo-EM maps with or without E-tRNA (see Methods) prepared as in **j**, **k** are shown at 3σ.

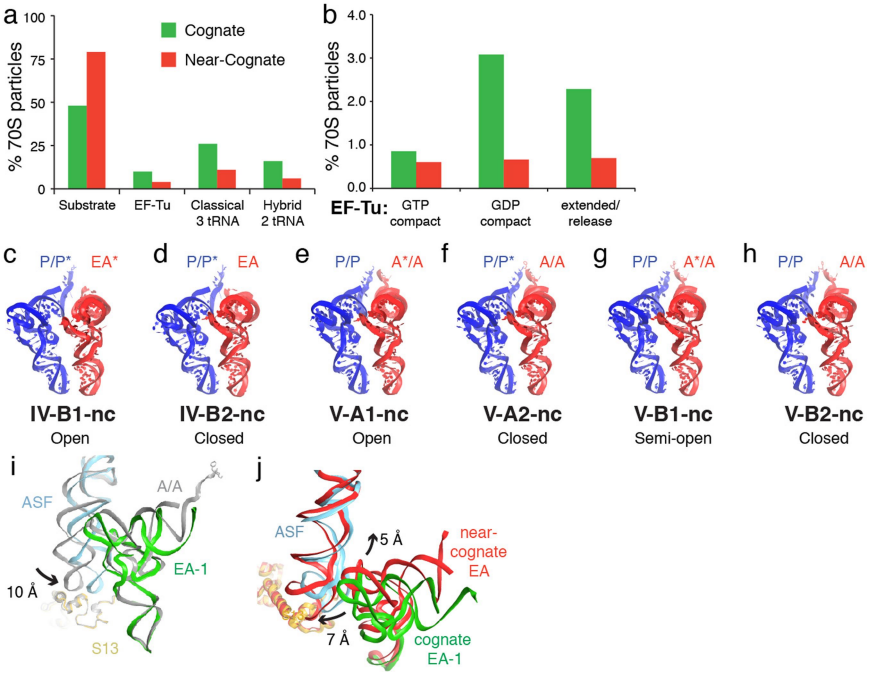

Extended Data Fig. 7 | Differences between near-cognate and cognate structural ensembles. a, Comparison of particle populations in cognate and near-cognate samples (at 30 s) reveals more substrate and less intermediate (EF-Tu) and product states for the near-cognate reaction. **b**, Near-cognate tRNA-bound EF-Tu is less abundant in GDP-bound states (after GTP hydrolysis) than the cognate complex. **c**, **d**, Elbow-accommodated EA tRNAs sample open (**c**) and closed (**d**) 30S conformations. **e**–**h**, CCA-accommodated tRNAs sample open and closed 30S conformations. Notably, state V-A1-nc, with an open 30S, shows a destabilized amino acid in the PTC. **i**, 30S-subunit partial rotation moves the ASF (cyan) in the cognate EA-1 and EA-2 states from their position in the EF-Tu release or accommodated A/A states (grey) allowing tRNA accommodation. **j**, Near-cognate tRNA (red) accommodation and interactions with the ASF differ from those of cognate tRNA (green).

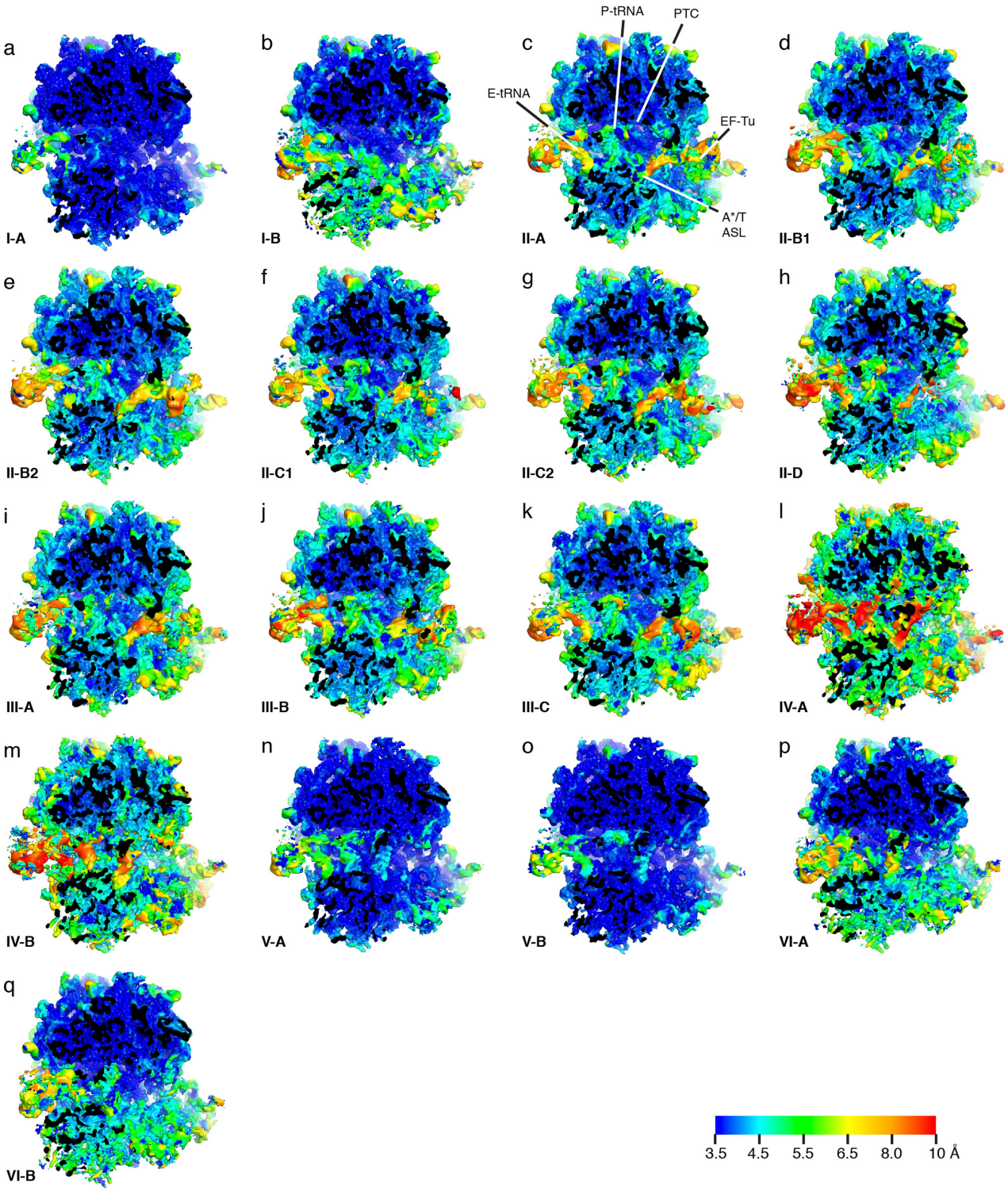

Extended Data Fig. 8 | Local resolutions of each cognate modelled class assessed by blocres. See Methods for details.

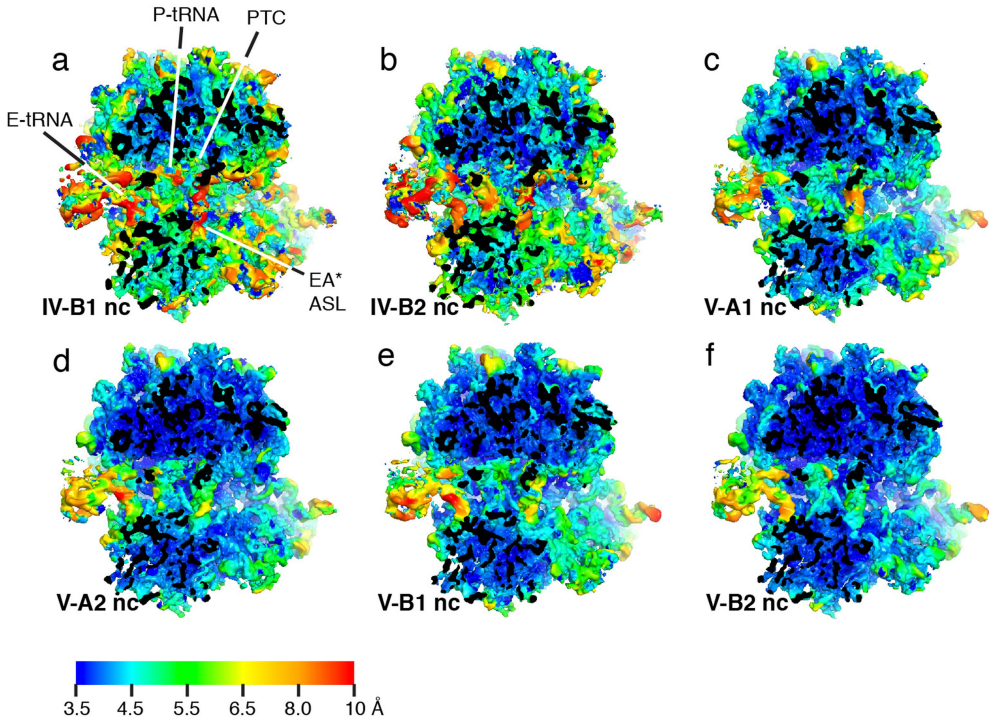

Extended Data Fig. 9 | Local resolutions of each near-cognate modelled class assessed by blocres. See Methods for details.

nature research

Corresponding author(s): Loveland, Anna B.
Korostelev, Andrei A.

Last updated by author(s): Mar 6, 2020

Reporting Summary

Nature Research wishes to improve the reproducibility of the work that we publish. This form provides structure for consistency and transparency in reporting. For further information on Nature Research policies, see Authors & Referees and the Editorial Policy Checklist.

Statistics

For all statistical analyses, confirm that the following items are present in the figure legend, table legend, main text, or Methods section.

n/a	Confirmed
☐	☒ The exact sample size (*n*) for each experimental group/condition, given as a discrete number and unit of measurement
☐	☒ A statement on whether measurements were taken from distinct samples or whether the same sample was measured repeatedly
☒	☐ The statistical test(s) used AND whether they are one- or two-sided *Only common tests should be described solely by name; describe more complex techniques in the Methods section.*
☒	☐ A description of all covariates tested
☒	☐ A description of any assumptions or corrections, such as tests of normality and adjustment for multiple comparisons
☒	☐ A full description of the statistical parameters including central tendency (e.g. means) or other basic estimates (e.g. regression coefficient) AND variation (e.g. standard deviation) or associated estimates of uncertainty (e.g. confidence intervals)
☒	☐ For null hypothesis testing, the test statistic (e.g. *F*, *t*, *r*) with confidence intervals, effect sizes, degrees of freedom and *P* value noted *Give P values as exact values whenever suitable.*
☒	☐ For Bayesian analysis, information on the choice of priors and Markov chain Monte Carlo settings
☒	☐ For hierarchical and complex designs, identification of the appropriate level for tests and full reporting of outcomes
☒	☐ Estimates of effect sizes (e.g. Cohen's *d*, Pearson's *r*), indicating how they were calculated

Our web collection on statistics for biologists contains articles on many of the points above.

Software and code

Policy information about availability of computer code

Data collection	Serial EM
Data analysis	Signature v.2, CTFFIND4 v., Frealign v. 9.11 (Aug 2017 release), cisTEM (version 1.0-beta and pre-release), EMAN(vs.2.07), Relion-(vs. 3-beta), Bsoft(1.9.1) (blocfilt/blocres), RSRef(2000), Phenix (1.16-3549), Chimera (vs. 1.7), MacPyMOL: PyMOL v1.7.0.5 enhanced for MacOsX, IMOD (vs. 4.9.0), SerialEM (vs. 3.6)

For manuscripts utilizing custom algorithms or software that are central to the research but not yet described in published literature, software must be made available to editors/reviewers. We strongly encourage code deposition in a community repository (e.g. GitHub). See the Nature Research guidelines for submitting code & software for further information.

Data

Policy information about availability of data

All manuscripts must include a data availability statement. This statement should provide the following information, where applicable:

- Accession codes, unique identifiers, or web links for publicly available datasets
- A list of figures that have associated raw data
- A description of any restrictions on data availability

The models generated and analyzed during the current study will be available from the RCSB Protein Data Bank: 6WD0 (Structure I-A), 6WD1 (Structure I-B), 6WD2 (Structure II-A), 6WD3 (Structure II-B1), 6WD4 (Structure II-B2), 6WD5 (Structure II-C1), 6WD6 (Structure II-C2), 6WD7 (Structure II-D), 6WD8 (Structure III-A), 6WD9 (Structure III-B), 6WDA (Structure III-C), 6WDB (Structure IV-A), 6WDC (Structure IV-B), 6WDD (Structure V-A), 6WDE (Structure V-B), 6WDF (Structure VI-A), 6WDG (Structure VI-B), 6WDH (Structure IV-B1-nc), 6WDI (Structure IV-B2-nc), 6WDJ (Structure V-A1-nc), 6WDK (Structure V-A2-nc), 6WDL (Structure V-B1-nc), and 6WDM (Structure V-B2-nc). The cryo-EM maps used to generate models will be available from the Electron Microscopy Databased: EMD-21619 (Structure I-A), EMD-21620 (Structure I-B), EMD-21621 (Structure II-A), EMD-21622 (Structure II-B1), EMD-21623 (Structure II-B2), EMD-21624 (Structure II-C1), EMD-21625 (Structure II-C2), EMD-21626 (Structure II-D), EMD-21627 (Structure III-A), EMD-21628 (Structure III-B), EMD-21629 (Structure III-C), EMD-21630 (Structure IV-A), EMD-21631 (Structure IV-B), EMD-21632 (Structure V-A), EMD-21633 (Structure V-B), EMD-21634 (Structure VI-A), EMD-21635 (Structure VI-B), EMD-21636

(Structure IV-B1-nc), EMD-21637 (Structure IV-B2-nc), EMD-21638 (Structure V-A1-nc), EMD-21639 (Structure V-A2-nc), EMD-21640 (Structure V-B1-nc), and EMD-21641 (Structure V-B2-nc).

Field-specific reporting

Please select the one below that is the best fit for your research. If you are not sure, read the appropriate sections before making your selection.

☒ Life sciences ☐ Behavioural & social sciences ☐ Ecological, evolutionary & environmental sciences

For a reference copy of the document with all sections, see nature.com/documents/nr-reporting-summary-flat.pdf

Life sciences study design

All studies must disclose on these points even when the disclosure is negative.

Sample size	Cryo-EM Datasets for cognate and near-cognate complexes were collected such that for intermediate timepoints EF-Tu-bound ribosomes could be detected and yield classes with at least 1000 particles to achieve ~4 A resolution. In practice datasets of ~100,000-700,000 particles were sufficient.
Data exclusions	As is typical practice in the cryo-EM field, pre-established exclusion criteria are to exclude images with bad ice or too much particle motion. Early datasets, in which we were establishing the conditions for the time-resolved study and which were performed under different conditons such as different stoichiometric of ribosomes to ternary complex components or very early timepoints (<5s, and that did not include EF-Tu bound to ribosomes, were excluded.
Replication	The high resolution cryo-EM data reported comes from a single experiment in which the time between mixing and plunging was varied to observe a time course. Earlier experiments collected on lower-end microscopes established that ternary complex could be found on the ribosome at ~15-60s when mixed under similar conditions. These are explained in the Methods.
Randomization	Computational approaches to unbiased particle classification (maximum likelihood classification) include randomizations. Classifications were repeated multiple times each varying number of classes or mask position.
Blinding	Blinding was not required because for each time point the structural data were all analyzed using the same methods.

Reporting for specific materials, systems and methods

We require information from authors about some types of materials, experimental systems and methods used in many studies. Here, indicate whether each material, system or method listed is relevant to your study. If you are not sure if a list item applies to your research, read the appropriate section before selecting a response.

Materials & experimental systems

n/a	Involved in the study
☒	☐ Antibodies
☒	☐ Eukaryotic cell lines
☒	☐ Palaeontology
☒	☐ Animals and other organisms
☒	☐ Human research participants
☒	☐ Clinical data

Methods

n/a	Involved in the study
☒	☐ ChIP-seq
☒	☐ Flow cytometry
☒	☐ MRI-based neuroimaging